Journal of *Marine Science and Engineering*

MDPI

Article

A Semi-Analytical Model for Studying Hydroelastic Behaviour of a Cylindrical Net Cage under Wave Action

Mingyuan Ma [1,2], Hong Zhang [1,2,*], Dong-Sheng Jeng [1] and Chien Ming Wang [3]

[1] School of Engineering and Built Environment, Griffith University, Gold Coast, QLD 4222, Australia; mingyuan.ma@griffithuni.edu.au (M.M.); d.jeng@griffith.edu.au (D.-S.J.)
[2] Cities Research Institute, Griffith University, Gold Coast, QLD 4222, Australia
[3] School of Civil Engineering, The University of Queensland, St. Lucia, QLD 4072, Australia; cm.wang@uq.edu.au
* Correspondence: hong.zhang@griffith.edu.au

Abstract: In the present study, a semi-analytical model based on the small-amplitude wave theory is developed to describe the wave fields around a single gravity-type cylindrical open fish net cage. The cage may be submerged to different depths below the free-water surface. The fish cage net is modelled as a flexible porous membrane, and the deflection of the net chamber is expressed by the transverse vibration equation of strings. The velocity potential is expanded in the form of the Fourier–Bessel series and the unknown coefficients in these series are determined from matching the boundary conditions and the least squares method. The number of terms for the series solution to be used is determined from convergence studies. The model results exhibit significant hydroelastic characteristics of the net cages, including the distribution properties of wave surface, pressure drop at the net interface, structural deflection, and wave loading along the cage height. In addition, the relationships between wave forces on the net cage with hydrodynamic and structural parameters are also revealed. The findings presented herein should be useful to engineers who are designing fish cage systems.

Keywords: fish net cage; hydroelastic analysis; potential flow model; wave scattering; Fourier–Bessel series; porous medium theory

Citation: Ma, M.; Zhang, H.; Jeng, D.-S.; Wang, C.M. A Semi-Analytical Model for Studying Hydroelastic Behaviour of a Cylindrical Net Cage under Wave Action. *J. Mar. Sci. Eng.* **2021**, *9*, 1445. https://doi.org/10.3390/jmse9121445

Academic Editors: Spyros A. Mavrakos and Dimitrios N. Konispoliatis

Received: 28 November 2021
Accepted: 11 December 2021
Published: 16 December 2021

1. Introduction

Fish farming not only provides an important protein supply for humans but also brings huge economic benefits. Average data from 2015 to 2017 indicates that fish products provide at least 20% of the animal protein intake of 3.3 billion people [1], and aquatic products accounted for about 46.4% of the food and agriculture production in 2017 [2]. In addition, the aquaculture industry of Australia is in a stage of rapid development and reached an annual output value of AUD 3.3 billion in 2020 [3]. In order to guarantee a stable output, the fishing cage system requires excellent reliability under environmental loads, such as waves and currents. Therefore, suitable modelling and studies on the dynamic response of the net cage to waves are crucial.

In many studies, the dynamic behaviour of fish cage nets is simulated by numerical models, for example, the bar element model in [4,5] or mass-spring model in [6,7], in which the hydrodynamic force on each element is estimated by the Morison equation or the screen-type method proposed by [8]. However, these models neglect the interferences of the structure and its motions on the flow field. For this reason, some researchers, e.g., Bi et al. [9] and Martin et al. [10], introduced computational fluid dynamics (CFD) techniques to achieve a fluid–structure interaction (FSI), but this requires tremendous computational time. In [10], it is reported that the simulation of a semisubmersible cage in irregular waves by FSI takes around 185 h for 300 s of simulation time on 64 cores (Intel Sandy Bridge) with 2.6 Ghz and 2 GB memory per core. This is not feasible to model a full-scale

fish net cage in detail in engineering practice. If some characteristics of the wave passing through the net can be simplified and solved analytically, then the computational time can be reduced significantly.

Usually, in theoretical analysis that allows for interaction between net cage and waves, the wave field is described by the linear potential flow theory, and the fish cage net is modelled as a porous medium membrane. The porous wavemaker theory is proposed by Chwang [11] to analyse the water wave generated by the harmonic oscillation of a vertical porous barrier, where the porous flow is described by Darcy's law. With the eigenfunction expansion and matching the boundary conditions, the particular solution of the velocity potential can be derived for the scattering issue of small-amplitude waves passing through permeable barriers in [12,13]. In terms of the interference effects among multiple rigid porous cylinders in waves, the scattering potential of each body in different local coordinates can be transformed by Graf's addition theorem in [14,15]. Furthermore, if waves interact with flexible structures, the motion of the structure can be approximately described by the vibration equation of the continuum according to [16–18].

Recently, some studies have adopted the aforementioned theoretical approaches to analyse the interaction between waves and net cages. The transverse displacement of the circular cage is assumed to be governed by the vibration equation of the elastic beam in [19,20], and the deflection of the horizontal net plate can be described by the two-dimensional membrane vibration equation, which was introduced by [21]. Selvan et al. [22] extend the theory of [21] to the interference effect of multiple cages. Furthermore, Guo et al. [23] present a detailed review about the mathematical modelling of wave interaction with flexible net-type structures.

Moreover, a few researchers employed numerical techniques based on the linear potential flow theory to investigate the wave–structure interaction problems. The scaled boundary finite element model is applied to investigate the interaction mechanism between waves and pile groups with arbitrary spatial layouts and cross-sections in [24]. A hybrid method is adopted to evaluate the wave force acting on a cube net cage in [25], where the velocity potential of the far-field wave is expressed in the Fourier–Bessel series, and the ambient waves are solved by Green's theorem, i.e., the boundary element method (BEM). In [26], the BEM and the Morison equation are combined to investigate the hydrodynamic characteristics of a semisubmersible aquaculture facility. The numerical and experimental comparisons in [25,26] both show acceptable agreement.

Based on the above literature review, several research gaps are identified. Firstly, when evaluating hydrodynamic loads with empirical models (Morrison equations or screen type methods), the wave field distribution induced by diffraction and radiation effects around the net cage has to be determined. Secondly, fish net cages may be designed with submerged capabilities to avoid strong surface waves. However, the above analytical models from [20–22] do not consider this scenario. Thirdly, for the net cage exposed to a wave field, knowledge about its hydroelastic behaviours is scarce. Therefore, it is essential to establish an analytical model to predict some key factors that determine the wave responses of fish net cages.

In the present study, the interactions between waves and submersible cylindrical fish net cage are approximated by a semi-analytical solution based on linear hydroelastic theory. The characteristics of the cage response to wave (free-water surface, pressure, hydrodynamic load, structural motion, etc.) are to be determined. This information is crucial for the design and application of fish cages. The linear model has advantages in the derivation of analytical solutions even if the boundary value problem is relatively complicated. The potential flow theory is also convenient for dealing with the domain with an infinite boundary, which means that an extremely large wave field is feasible to be analysed. The paper is arranged as follows: Section 2 presents the assumptions, modelling, governing equation, and boundary conditions for the wave–cage interaction problem. In Section 3, the method of solution for the governing equations and boundary value problems is elaborated. Section 4 presents the convergence studies and model validation.

Section 5 presents the calculated results and explains the hydroelastic behaviour of the net cage under wave action. In Section 6, parametric studies are established to reveal the relationship between the wave force on the net cage and various hydrodynamic and structural parameters. Finally, brief conclusions are given in Section 7.

2. Problem Definition, Assumptions, Modelling, Governing Equation, and Boundary Conditions

In this study, a cylindrical net cage is considered as shown in Figure 1, and it is convenient to describe the physical problem in a cylindrical coordinate system (r, θ, z). A small-amplitude wave propagates along the direction of $\theta = 0$ with a circular frequency ω and a wave height H. The mean water level is at $z = 0$, and the cage is submerged in a finite water depth of h. The central axis of the cage with a height of d_2 is located at the position $r = 0$, and its top end can be submerged below the mean water level in d_1. In addition, the top end is constrained by mooring systems at $z = -d_1$, whilst the bottom end of $z = -(d_1 + d_2)$ is free.

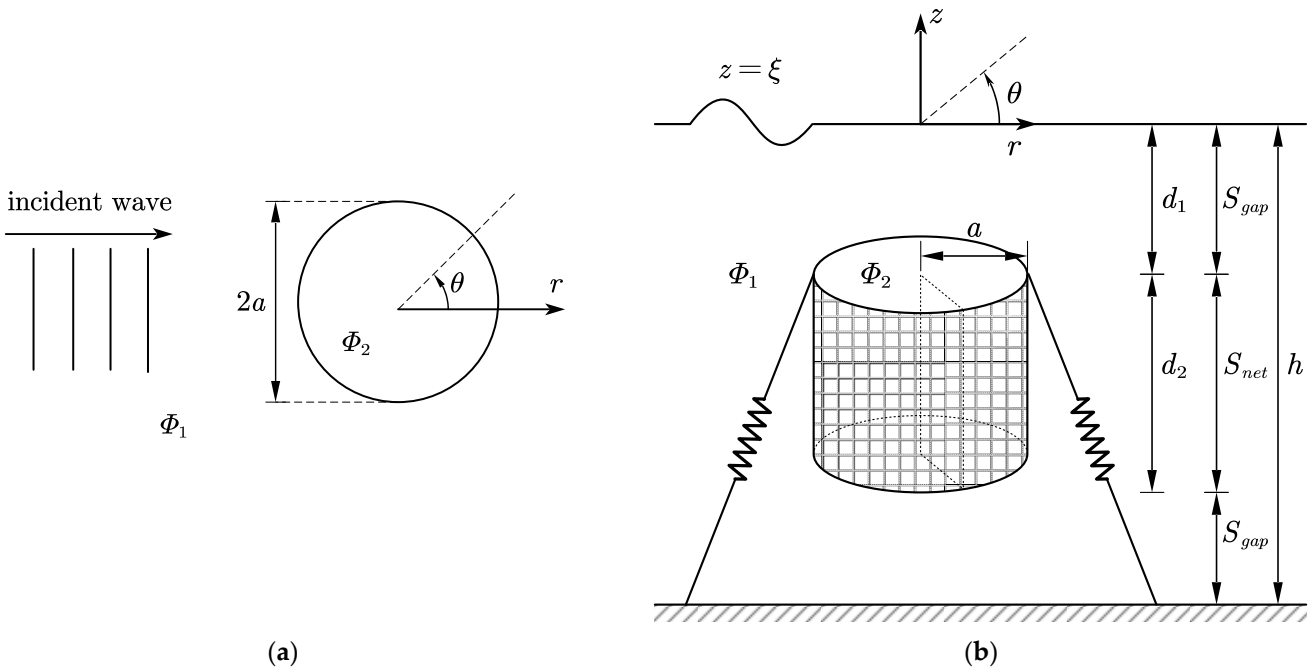

Figure 1. A sketch of a cylindrical net cage submerged in a finite water depth: (**a**) plan view. (**b**) side view.

The flow domain may be divided into two zones: Region 1 ($r > a$, $-h < z < 0$) is the external region outside the net cage, while Region 2 ($r < a$, $-h < z < 0$) is the area within the circular net chamber. For the structural domain, the notations S_{net} and S_{gap} represent the net region of $-(d_1 + d_2) \leq z \leq d_1$ and the gap portions of $-d_1 < z \leq 0 \cup -h \leq z < -(d_1 + d_2)$, respectively.

The problem at hand is to determine the hydroelastic behaviour of the submerged cylindrical net cage under wave action.

2.1. Governing Equations

Assuming that the fluid is incompressible, irrotational, and inviscid, Φ_1 and Φ_2 represent the velocity potentials in Regions 1 and 2, respectively, and the velocity potential $\Phi_j\,(r, \theta, z, t)$ $(j = 1, 2)$ can be written as

$$\Phi_j = \text{Re}\left[\varphi_j(r, \theta, z)e^{-\text{i}\omega t}\right], \tag{1}$$

where φ_j is the spatial component of the velocity potential, and it is governed by the Laplace equation in the cylindrical coordinate:

$$\frac{\partial^2 \varphi_j}{\partial r} + \frac{1}{r}\frac{\partial \varphi_j}{\partial r} + \frac{1}{r^2}\frac{\partial^2 \varphi_j}{\partial \theta} + \frac{\partial^2 \varphi_j}{\partial z^2} = 0. \tag{2}$$

In addition, φ_j can be represented as a superposition of the incident wave component φ^I and the scattered (diffraction and radiation) wave component φ_j^S, i.e.,

$$\varphi_j = \varphi^I + \varphi_j^S. \tag{3}$$

2.2. Boundary Conditions

At the free-water surface $z = \xi$, the linearised kinematic free surface (**KFSBC**) boundary condition satisfies

$$\frac{\partial \Phi_j}{\partial z} = \frac{\partial \xi}{\partial t}, \text{ at } z = 0, \tag{4a}$$

and dynamic free surface boundary condition (**DFSBC**) is

$$\xi = -\frac{1}{g}\frac{\partial \Phi_j}{\partial t}, \text{ at } z = 0. \tag{4b}$$

By combining Equation (4a,b), the boundary condition at the mean water level is

$$\frac{\partial \varphi_j}{\partial z} - \frac{\omega^2}{g}\varphi_j = 0, \text{ at } z = 0, \tag{4c}$$

and the slip boundary condition on the seabed is given by

$$\frac{\partial \varphi_j}{\partial z} = 0, \text{ at } z = -h. \tag{5}$$

Furthermore, the scattered potential component φ_j^S satisfies the Sommerfeld radiation condition when r approaches infinity [27], i.e.,

$$\lim_{r\to\infty} \sqrt{r}\left(\frac{\partial \varphi_1^S}{\partial r} - \mathrm{i}k_0\varphi_1^S\right) = 0, \tag{6}$$

where k_0 is the incident wavenumber.

As shown in Figure 2, the cage net is modelled as a porous membrane, so the penetrated flow through the net interface satisfies the linearised kinematic condition:

$$\frac{\partial \varphi_j}{\partial r} = \mathrm{i}\sigma(\varphi_2 - \varphi_1) - \mathrm{i}\omega\eta cos\theta, \text{ at } r = a \text{ and } z \in S_{\text{net}}, \tag{7}$$

in which η is the spatial component of the transverse deflection of the cage along the incident direction of the wave, and σ is the porous-effect parameter of the net that is expressed by an empirical formula given by Ito et al. [25]:

$$\sigma = (1 + \mathrm{i}\sigma_i)\sigma_r \tag{8a}$$

$$\sigma_r = \frac{k_0}{2\pi} \times \frac{(27.73/\varepsilon + 469.0)G^2}{1 + (0.5510 - 0.01998/\varepsilon)G}, \tag{8b}$$

where G is the opening ratio of the net, ε is the incident wave slope $Hk_0/2$, and the imaginary part of σ represents the fluid inertia effect. A high Keulegan–Carpenter number indicates a minor fluid inertia effect compared to the fluid drag effect. In [7], for the net twine with a diameter of a few millimetres, its KC (Keulegan–Carpenter) number is 160 to 350 based on

the laboratory tests, and the wave-induced inertia force is considered negligible compared to its drag force on the fish net. In the real sea condition, higher wave height and wave periods also mean a greater KC number. Currently, there is no appropriate formula of σ_i given for the cylindrical net cage; therefore, it is taken as 0 if there is no special explanation. Notably, the influence of σ_i is discussed in Section 6.

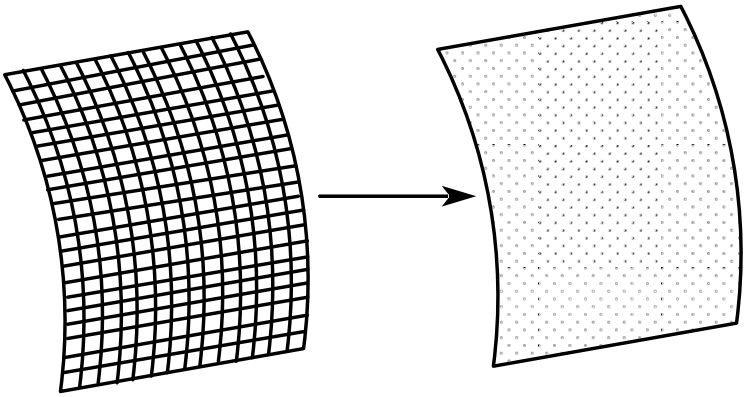

Figure 2. The fish net is modelled as a porous membrane.

In addition, the continuity of the normal velocity and pressure of the flow at the interface between Regions 1 and 2 requires

$$\frac{\partial \varphi_1}{\partial r} = \frac{\partial \varphi_2}{\partial r}, \text{ at } r = a, -h < z < 0, \tag{9a}$$

$$\varphi_1 = \varphi_2, \text{ at } r = a \text{ and } z \in S_{gap}. \tag{9b}$$

On the other hand, it is assumed that the cross-section of the cage maintains its circular shape under wave action if the cage is imposed a high axial tension and has a small deformation relative to its overall size. Liu et al. [28] showed a deformed net cage simulated by the finite element method using truss elements, and it is observed that the cage approximately maintains a circular cross-section. Therefore, the transverse deflection of the cage is $\zeta = \mathrm{Re}[\eta(z)e^{-i\omega t}]$, and the transverse vibration equation of the string to describe the complex amplitude η is given by Mandal and Sahoo [21]:

$$\frac{d^2\eta}{dz^2} + \frac{m_s\omega^2}{Q}\eta = -\frac{ai\omega\rho}{Q}\int_0^{2\pi}(\varphi_1 - \varphi_2)\cos(\pi - \theta)d\theta, \tag{10}$$

in which Q is the axial uniform tensile force in the net, m_s is the uniform mass of the net per unit length, and ρ is the water density. In [28], a comparison between the analytical model based on Equation (10) and the FEM simulation for the cylindrical net cage illustrates acceptable errors.

For the edge restraint condition of the net chamber, its top end is assumed to be constrained by the mooring systems according to [28], and there is no transverse traction at the bottom end, i.e.,

$$Q\frac{d\eta}{dz} = k_s\eta, \text{ at } z = -d_1, \tag{11a}$$

$$\frac{d\eta}{dz} = 0, \text{ at } z = -(d_1 + d_2). \tag{11b}$$

where k_s is the spring constant of the mooring cables.

3. Method of Solutions

In view of the governing equation, Equation (2), and the boundary conditions, Equations (4c), (5), and (6), the solution of φ_1 is sought in the form

$$\varphi_1 = \varphi_I + \varphi_1^S, \tag{12a}$$

where

$$\varphi_I = \sum_{m=0}^{\infty} -\frac{igH}{2\omega}\frac{\cosh[k_0(z+h)]}{\cosh(k_0h)}\mu_m J_m(k_0r)\cos(m\theta), \tag{12b}$$

$$\mu_m = \begin{cases} 1, & m=0 \\ 2i^m, & m>0 \end{cases}, \tag{12c}$$

$$\varphi_1^S = \sum_{m=0}^{\infty}\sum_{n=0}^{\infty} A_{mn}R_m^1(k_nr)f_n(z)\cos(m\theta), \tag{12d}$$

$$R_m^1(k_nr) = \begin{cases} \frac{H_m(k_nr)}{H_m'(k_na)}, & n=0 \\ \frac{K_m(k_nr)}{K_m'(k_na)}, & n>0 \end{cases}, \tag{12e}$$

$$f_n(z) = \begin{cases} \frac{\cosh[k_n(z+h)]}{\cosh(k_nh)}, & n=0 \\ \frac{\cos[k_n(z+h)]}{\cos(k_nh)}, & n>0 \end{cases}. \tag{12f}$$

Similarly, according to the governing equation, Equation (2), and the boundary conditions, Equations (4c) and (5), the general solution of φ_2 is

$$\varphi_1 = \varphi_I + \varphi_1^S, \tag{13a}$$

where

$$\varphi_2^S = \sum_{m=0}^{\infty}\sum_{n=0}^{\infty} B_{mn}R_m^2(k_nr)f_n(z)\cos(m\theta), \tag{13b}$$

$$R_m^2(k_nr) = \begin{cases} \frac{J_m(k_nr)}{J_m'(k_na)}, & n=0 \\ \frac{I_m(k_nr)}{I_m'(k_na)}, & n>0 \end{cases}. \tag{13c}$$

k_ns are the real roots of the following dispersion relations:

$$\begin{cases} \omega^2 = gk_n\tanh(k_nh), & n=0 \\ \omega^2 = -gk_n\tan(k_nh), & n>0 \end{cases}, \tag{14}$$

and A_{mn} and B_{mn} are the unknown constants, J_m is the first kind of Bessel function, H_m is the first kind of Hankel function, I_m is the first kind of modified Bessel function, and K_m is the second kind of modified Bessel function, where the subscript m is the order of the Bessel function.

By substituting Equations (12a–f) and (13a–c) into the boundary condition Equation (9a) and applying the orthogonality operation of $\cosh[k_n(z+h)]$, $\cos(k_nh)$, $n = 0, 1, 2\ldots$ over $-h \le z \le 0$ and $\cos(m\theta)$, $m = 0, 1, 2\ldots$ over $0 \le \theta \le 2\pi$, the unknown constants in Equations (12d) and (13b) satisfy

$$A_{mn} = B_{mn}. \tag{15}$$

Therefore, one can write

$$\Delta\varphi = \varphi_1 - \varphi_2 = \sum_{m=0}^{\infty}\sum_{n=0}^{\infty} A_{mn}X_{mn}f_n(z)\cos(m\theta), \text{ at } r=a, \tag{16a}$$

where

$$X_{mn} = R_m^1(k_na) - R_m^2(k_na). \tag{16b}$$

By substituting Equation (16a,b) into Equation (10) and noting the orthogonality of $\cos(m\theta)$, $m = 0, 1, 2 \ldots$ over $0 \le \theta \le 2\pi$, Equation (10) might be rewritten as

$$\frac{d^2\eta}{dz^2} + \alpha_1\eta = \alpha_2 \sum_{n=0}^{\infty} A_{1n}X_{1n}f_n(z), \tag{17a}$$

where

$$\alpha_1 = m_s\omega^2/Q \text{ and } \alpha_2 = \pi a i\omega\rho/Q. \tag{17b}$$

Therefore, the general solution for $\eta(z)$ is

$$\eta(z) = \sum_{\kappa=1}^{2} C_\kappa e^{q_\kappa z} + \sum_{n=0}^{\infty} A_{1n}F_n f_n(z), \tag{18a}$$

in which

$$F_n = \begin{cases} \frac{\alpha_2 X_{1n}}{\alpha_1 + k_n^2}, & n = 0 \\ \frac{\alpha_2 X_{1n}}{\alpha_1 - k_n^2}, & n > 0 \end{cases}, \tag{18b}$$

and q_κs are the roots of the characteristic equation of Equation (17a), and they are given by

$$q_1 = \mathrm{i}\omega\sqrt{m_s/Q} \text{ and } q_2 = -\mathrm{i}\omega\sqrt{m_s/Q}. \tag{18c}$$

By substituting Equation (18a–c) into the boundary condition, Equation (11a,b), the constant C_κs are acquired through

$$\begin{cases} \sum_{\kappa=1}^{2} C_\kappa(k_s - qQ)e^{-q_\kappa d_1} + \sum_{n=0}^{\infty} A_{1n}[k_s F_n f_n(-d_1) - QF_n f_n'(-d_1)] = 0 \\ \sum_{\kappa=1}^{2} C_\kappa q_\kappa e^{-q_\kappa(d_1+d_2)} + \sum_{n=0}^{\infty} A_{1n}F_n f_n'[-(d_1+d_2)] = 0 \end{cases}. \tag{19}$$

For the net portion $z \in S_{net}$, substituting Equations (12a–f), (16a,b), and (18a–c) into Equation (7) and invoking the orthogonality of $\cos(m\theta)$ again, one obtains,

when $m \neq 1$,

$$\sum_{n=0}^{\infty} A_{mn}k_n f_n(z) + \mathrm{i}\sigma \sum_{n=0}^{\infty} A_{mn}X_{mn}f_n(z) - \frac{\mathrm{i}gHk_0}{2\omega}\frac{\cosh[k_0(z+h)]}{\cosh(k_0h)}\mu_m J_m'(k_0a) = 0, \tag{20a}$$

and when $m = 1$,

$$\begin{gathered} \sum_{n=0}^{\infty} A_{1n}k_n f_n(z) + \mathrm{i}\sigma \sum_{n=0}^{\infty} A_{1n}X_{1n}f_n(z) + \mathrm{i}\omega \sum_{n=0}^{\infty} A_{1n}F_n f_n(z) - \\ \frac{\mathrm{i}gHk_0}{2\omega}\frac{\cosh[k_0(z+h)]}{\cosh(k_0h)}\mu_m J_m'(k_0a) + \mathrm{i}\omega \sum_{j=1}^{2} C_\kappa e^{q_\kappa z} = 0. \end{gathered} \tag{20b}$$

For the gap portion $z \in S_{gap}$, substituting Equation (16a) into Equation (9b) and using the orthogonality of $\cos(m\theta)$ yields

$$\sum_{n=0}^{\infty} A_{mn}X_{mn}f_n(z) = 0. \tag{21}$$

As a result, a system of equations can be obtained from Equations (20a,b) and (21):

$$S_m(z) = \sum_{n=0}^{\infty} A_{mn}\epsilon_{mn}(z) + \lambda_m(z) = 0, \tag{22a}$$

where, when $m \neq 1$,

$$\epsilon_{mn}(z) = \begin{cases} (k_n + \mathrm{i}\sigma X_{mn})f_n(z), & z \in S_{net} \\ X_{mn}f_n(z), & z \in S_{gap} \end{cases}, \tag{22b}$$

$$\lambda_m(z) = \begin{cases} -\frac{\mathrm{i}gHk_0}{2\omega}\frac{\cosh[k_0(z+h)]}{\cosh(k_0h)}\mu_m J_m'(k_0a), & z \in S_{net} \\ 0, & z \in S_{gap} \end{cases}, \tag{22c}$$

and when $m = 1$,

$$\epsilon_{mn}(z) = \begin{cases} (k_n + \mathrm{i}\sigma X_{mn} + \mathrm{i}\omega F_n) f_n(z), & z \in S_{net} \\ X_{mn} f_n(z), & z \in S_{gap} \end{cases}, \tag{22d}$$

$$\lambda_m(z) = \begin{cases} -\frac{\mathrm{i}gHk_0}{2\omega} \frac{\cosh[k_0(z+h)]}{\cosh(k_0 h)} \mu_m J'_m(k_0 a) + i\omega \sum_{j=1}^{2} C_\kappa e^{q_\kappa z}, & z \in S_{net} \\ 0, & z \in S_{gap} \end{cases}. \tag{22e}$$

Truncating the infinite series after N^{th} terms in Equation (22a) yields

$$S_m(z) = \sum_{n=0}^{N} A_{mn} \epsilon_{mn}(z) + \lambda_m(z) = 0. \tag{23}$$

By manipulating the least-squares approximation for Equation (23), one obtains

$$\int_{-h}^{0} |S_m(z)|^2 dz = min \Rightarrow \int_{-h}^{0} S_m^* \frac{\partial S(z)}{\partial A_{mn}} dz = 0, \tag{24}$$

and a system of equations about A_{mn} is acquired by substituting Equation (23) into Equation (24):

$$\sum_{n=0}^{N} A_{mn}^* \Psi_{mn,l} = \Omega_{m.l}, \tag{25a}$$

where

$$\Psi_{mn,l} = \int_{-h}^{0} \epsilon_{mn}^* \epsilon_{m,l} dz \text{ and } \Omega_{m,l} = -\int_{-h}^{0} \lambda_m^* \epsilon_{m,l} dz, \tag{25b}$$

and $m = 0, 1, 2, \ldots, M$; $l = 0, 1, 2, \ldots, N$.

Therefore, A_{mn} and C_κ are solved by combining Equations (19) and (25a,b), and the complex amplitude of the velocity potential φ_j is calculated from Equations (12a–f) and (13a–c).

Finally, in view of the linearised Bernoulli's equation, the complex dynamic pressure p is

$$p_j = -\rho \frac{\partial(\varphi_j e^{-\mathrm{i}\omega t})}{\partial t}, \tag{26}$$

and the complex pressure difference acting on the net interface is defined as

$$\Delta p = p_1 - p_2, \text{ at } r = a. \tag{27}$$

As a result, the complex function of the horizontal hydrodynamic force per unit length along the cage height is given by

$$f(z) = a \int_0^{2\pi} \Delta p \cos(\pi - \theta) d\theta = -\pi a i \omega \rho \sum_{n=0}^{N} A_{1n} X_{1n} f_n(z) e^{-\mathrm{i}\omega t}, \tag{28}$$

and the wave force and the resulting overturning moment with respect to the top of the cage are

$$F = \int_{-(d_1+d_2)}^{-d_1} f(z) dz \text{ and } M_o = \int_{-(d_1+d_2)}^{-d_1} f(z) \left(z + d_1 + \frac{d_2}{2} \right) dz. \tag{29}$$

Furthermore, according to the **DFSBC**, Equation (4b), the free-water surface elevation ξ is given by

$$\xi_j = \mathrm{Re}\left(\frac{\mathrm{i}\omega \varphi_j e^{-\mathrm{i}\omega t}}{g} \right). \tag{30}$$

4. Convergence Studies and Model Validation

In Section 3, the derived solution is written in the form of the Fourier–Bessel series, and the infinite terms have been truncated after N^{th} and M^{th} terms. Theoretically, the

calculated result is only valid when the solution converges with the increasing number of the series term. Therefore, convergence studies are required to determine the truncated terms to use for accurate results. For the convergence studies, the following parameters are adopted: $H = 7$ m, $h = 200$ m, $a = 50$ m, $d_1 = 0$, $d_2 = 50$ m, and $G = 0.7$. The nondimensional mooring spring constant $\alpha = k_s/(m_s g)$ is 20, the nondimensional axial tensile force in the net $\gamma = Q/(m_s g d_2)$ is taken as 1, and the nondimensional net mass per unit length $\beta = m_s/(\rho {d_2}^2) = 0.001$. The wave frequency ω varies from 0.2 rad/s to 1.4 rad/s at an interval of 0.4 rad/s. In Equation (18a–c), due to the orthogonality of $\cos(m\theta)$, the convergence of η is only determined by the series term generated by the wavenumbers from the dispersion relation Equation (14), so a control error $\Delta Er\ (N)$ versus the truncated term N is defined as

$$\Delta E_r(N) = \frac{\left|\eta\left(-d_1 - \frac{d_2}{2}\right)_{,N+1} - \eta\left(-d_1 - \frac{d_2}{2}\right)_{,N}\right|}{\left|\eta\left(-d_1 - \frac{d_2}{2}\right)_{,N}\right|}. \tag{31}$$

The variations of $\Delta Er\ (N)$ versus N from 1 to 50 are shown in Figure 3a. The results exhibit different convergency speeds for different wave frequencies, and the values of $\Delta Er\ (N)$ converge more slowly when the wave frequency is larger. Notably, when $N > 30$, the maximum control error is less than 2.25% for all cases. Alternatively, for the solution of the local wave field near the cage, the control error $\Delta Er\ (M)$ versus the truncated term M is defined as follows:

$$\Delta E_r(M) = \frac{\left|\sum_{z=-(d_1+d_2)}^{-d_1} \sum_{\theta=0}^{2\pi} \Delta\varphi(a,\theta,z)_{,M+1} - \sum_{z=-(d_1+d_2)}^{-d_1} \sum_{\theta=0}^{2\pi} \Delta\varphi(a,\theta,z)_{,M}\right|}{\left|\sum_{z=-(d_1+d_2)}^{-d_1} \sum_{\theta=0}^{2\pi} \Delta\varphi(a,\theta,z)_{,M}\right|}. \tag{32}$$

The curves of $\Delta Er\ (M)$ versus M from 1 to 50 are presented in Figure 3b. Similarly, if the wave frequency is lower, the control error will show a more rapid decay, and the control errors of the whole cases are closed to 0 for when $M > 18$. Based on the convergence studies, it is sufficient to take $N = 30$ and $M = 20$ to guarantee the accuracy for the solution of the imposed wave action and cage displacement.

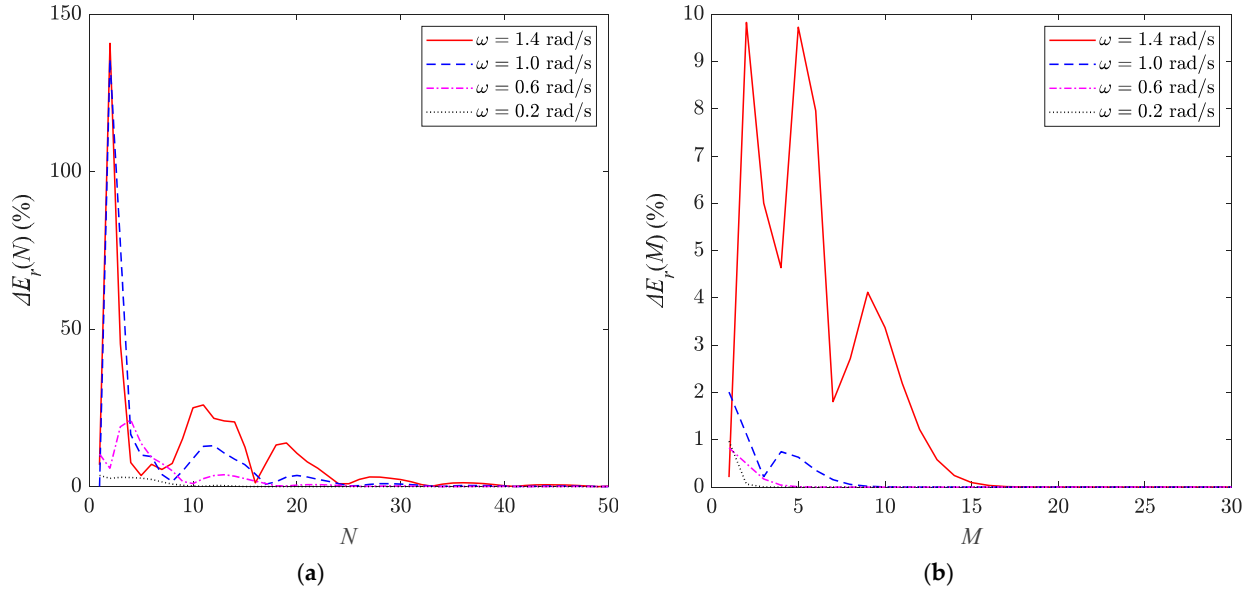

Figure 3. Convergence curves of control errors versus truncated terms for different wave frequencies: (**a**) $\Delta E_r\ (N)$ versus N; (**b**) $\Delta E_r\ (M)$ versus M.

In order to examine the correctness of the aforementioned formulations, consider a rigid impermeable or porous circular cage illustrated in [29,30] with the parameters of h = 5 m, a = 0.15 m, d_1 = 0, and d_2 = 0.3 m. The structural parameters adopted α = 1000, γ = 1000, and β = 1000 to ensure the cage motion is negligible. The nondimensional horizontal wave force acting on the cage versus the normalized wavenumber k_0a is shown in Figure 4a. There are no significant differences between the present model and the aforementioned studies. A small discrepancy observed is because a horizontal impermeable plate is considered at the bottom of the cage in [29,30]. In addition, the current analytical solution of the cage deflection amplitude $|\eta|$ is validated with the numerical solution generated by the Runge–Kutta method, where the parameters adopt the one in the convergence studies and ω = 1 rad/s. Figure 4b indicates that the derived analytical solution is completely consistent with the numerical results.

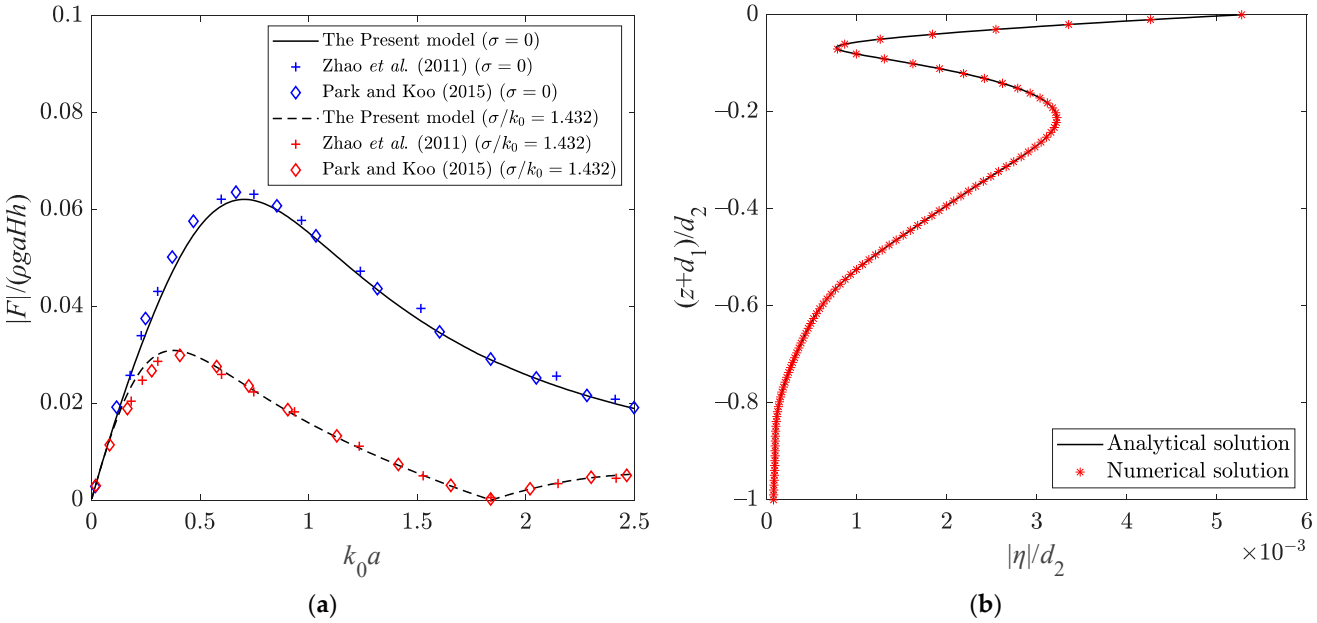

Figure 4. Model validations: (**a**) horizontal wave force $|F|$; (**b**) cage deflection amplitude $|\eta|$.

5. Hydroelastic Analysis of Fish Net Cage

This section discusses the hydroelastic spatial characteristics of the net cages by some numerical results. Five case groups were designed with various wave periods T (Cases A), net opening ratios G (Cases B), nondimensional mooring spring constants α (Cases C), nondimensional axial tensile forces γ in the net (Cases D), and immersed depths d_1 of the cage (Cases E). The detailed parameter settings are shown in Table 1. In this analysis, a full-scale cage deployed in the marine aquaculture industry is considered, in which the cage radius a = 50 m, the cage height d_2 = 50 m, and the dimensionless net mass per unit length β = 0.001. Moreover, the wave height H = 7 m and the water depth h = 200 m are adopted.

Table 1. Case group with different parameters.

Cases	T (s)	G	α	γ	d_1 (m)
A1	4	0.7	20	1	0
A2	6	0.7	20	1	0
A3	8	0.7	20	1	0
A4	10	0.7	20	1	0
B1	8	0.1	20	1	0
B2	8	0.2	20	1	0
B3	8	0.3	20	1	0
B4	8	0.4	20	1	0
B5	8	0.6	20	1	0
B6	8	0.7	20	1	0
B7	8	0.8	20	1	0
B8	8	0.9	20	1	0
C1	8	0.7	1	1	0
C2	8	0.7	10	1	0
C3	8	0.7	20	1	0
C4	8	0.7	Fixed end	1	0
D1	8	0.7	20	0.5	0
D2	8	0.7	20	1	0
D3	8	0.7	20	2	0
D4	8	0.7	20	4	0
E1	8	0.7	20	1	0
E2	8	0.7	20	1	10
E3	8	0.7	20	1	30
E4	8	0.7	20	1	50

5.1. Hydrodynamic Behaviours

The present model can evaluate the distribution of the velocity potential Φ of the fluid domain and then derive its corresponding dynamic pressure and free surface elevations at a series of discretised points. Here, Cartesian coordinates ($x = r\cos\theta$ and $y = r\sin\theta$) are established to facilitate the description of the results, where the central axis of the cage is located at the z-axis, and the incident wave propagates along the positive direction of the x-axis.

The free surface elevations ξ (m) around the cage with varied net opening ratios (Cases B1 to B4) are illustrated in Figure 5, in which ξ is calculated from Equation (30) in a domain of $x = \pm$ 200 m and $y = \pm$ 200 m. In this example, ξ adopted the values at time $t = nT$, $n = 0, 1, 2, \ldots, \infty$, and the black circle is the demarcation between Regions 1 and 2. It can be observed that the presence of the cage causes perturbations to the wave surface, especially for the cage with an impermeable interface (i.e., net opening ratio $G = 0$). The transmitted wave passing through the cage will be attenuated, and its amplitude will gradually restore to its original state. This occurs because, when the scattered wave radiates away from the cage, the scattering potential gradually decays. Alternatively, the wave surface in the inner region of the cage also has different extents of attenuation, and the energy dissipation is the most severe, especially when $G = 0$. It is worth noting that, due to the blocking effect of the porous net, the water surface elevation inside the cage is affected by a certain lag in propagation when compared with the waves outside the cage. Furthermore, when the opening ratio of the net is gradually increased, the disturbance of the cylindrical net to the wave surface will gradually become weak, and the observed wave scattering becomes relatively minor for the cases with $G > 0.3$. In engineering practice, the adopted opening ratio of the fish net is usually greater than 0.6, so the influence of the net cage on the wave surface has become weak at this time.

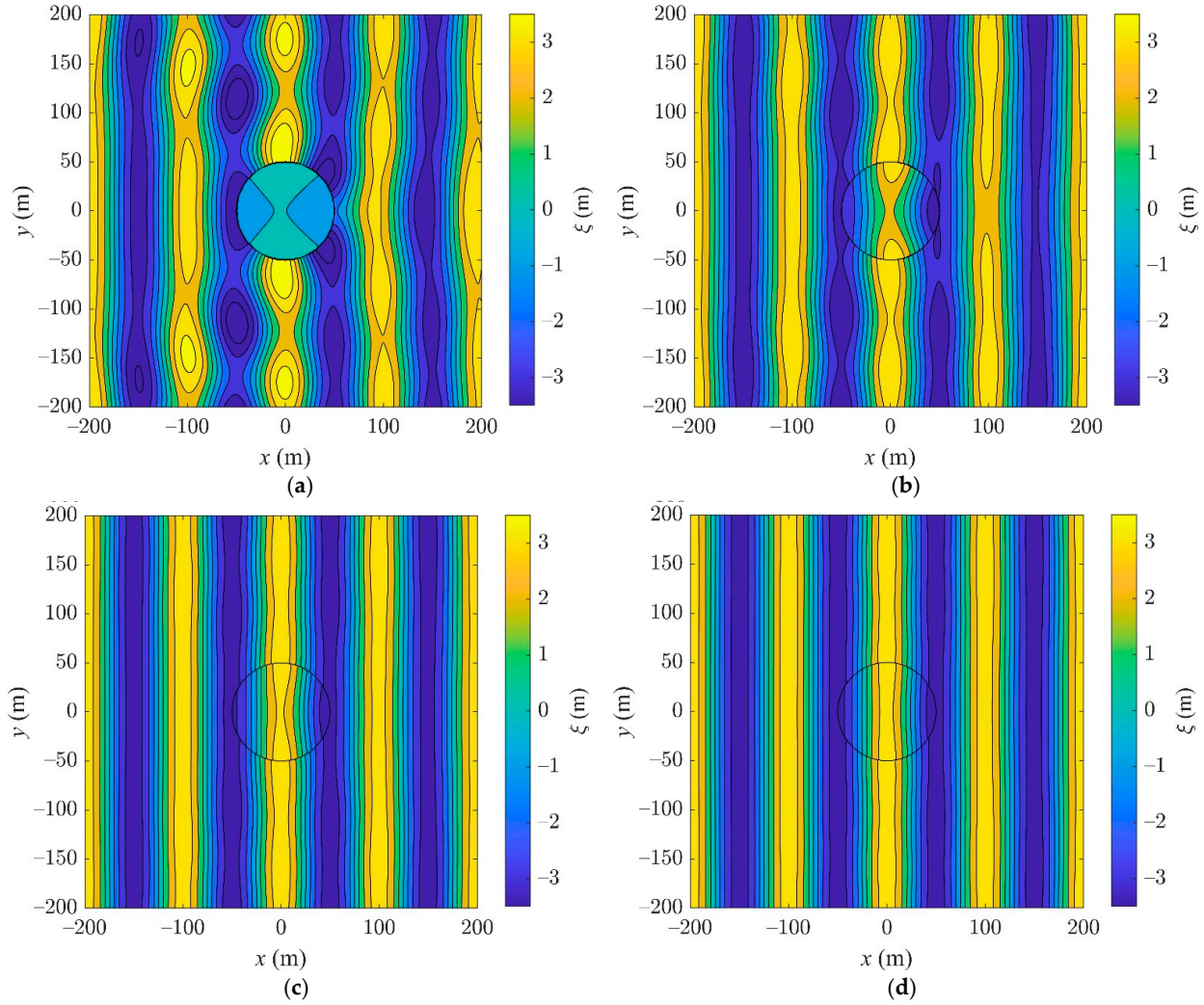

Figure 5. Free-water surface elevations ξ (m) around a cylindrical net cage with different opening ratios at $t = nT$, $n = 0, 1, 2, \ldots, \infty$, Cases B1 to B4: (**a**) $G = 0$. (**b**) $G = 0.1$. (**c**) $G = 0.2$. (**d**) $G = 0.3$.

Figure 6 shows the amplitude distributions of the pressure differences $|\Delta p|$ on the windward and leeward sides of the net chamber in the incident wave direction. $|\Delta p|$ is defined in Equation (27), and the results in Cases A1 to A4 with different wave periods are discussed. The maximum values of $|\Delta p|$ are mainly concentrated at the top of the cylindrical cage, in which the maximum values are greater when the wave periods are smaller, that is 1.20 kPa ($T = 4$ s), 1.13 kPa ($T = 6$ s), 1.04 kPa ($T = 8$ s), and 0.89 kPa ($T = 10$ s). Nevertheless, the values of $|\Delta p|$ at the lower part of the cage are relatively minor, and the values at its bottom end are close to 0. These results demonstrate that the wave has a more significant impact on the top part of the cage. Notably, more areas on the cage surface will withstand the pressure drop with high amplitudes under the wave action with longer periods, because short waves mainly concentrate on the free-water surface. Moreover, due to the energy dissipation of the transmitted wave, the pressure drop $|\Delta p|$ on the leeward side is also slightly higher.

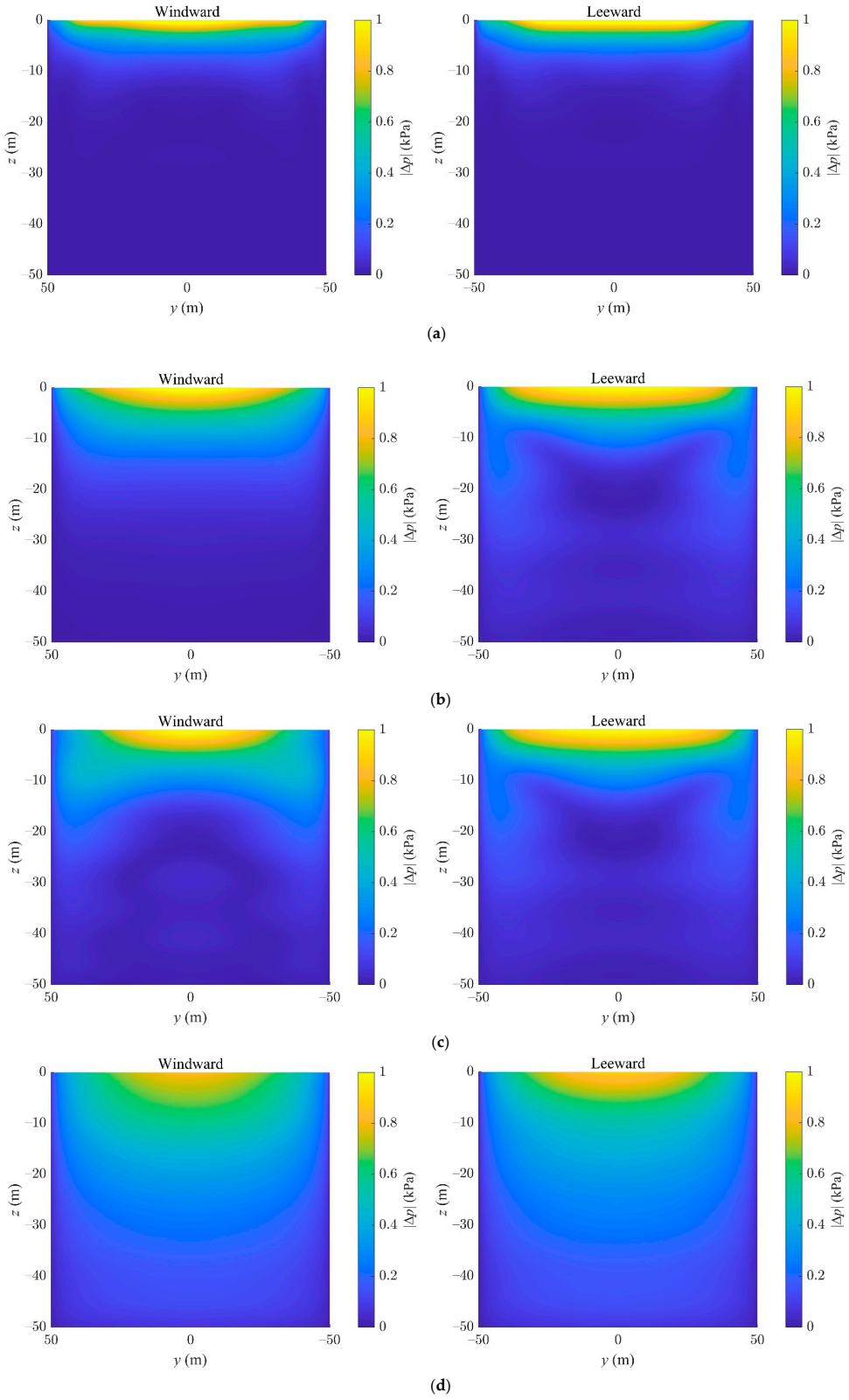

Figure 6. Amplitude distributions of dynamic pressure drop $|\Delta p|$ (kPa) on windward and leeward sides of the net interface in the wave propagating direction, Cases A1 to A4: (**a**) T = 4 s. (**b**) T = 6 s. (**c**) T = 8 s. (**d**) T = 10 s.

5.2. Structural Dynamic Responses

In this section, the structural dynamic responses of the net cage are investigated. Two important indices are presented: the nondimensional amplitude of the structural transverse deflection $|\eta|/d_2$, and the nondimensional amplitude of the horizontal wave load per unit length K_f along the cage height. Following in the work of Mandal and Sahoo [21], K_f is defined as

$$K_f = \frac{|f(z)|}{\rho g a H}, \tag{33}$$

in which the horizontal wave load per unit length $f(z)$ is found from Equation (28). The curves of $|\eta|/d_2$ and K_f versus the relative position defined as $(z + d_1)/d_2$ are plotted in Figures 7–11.

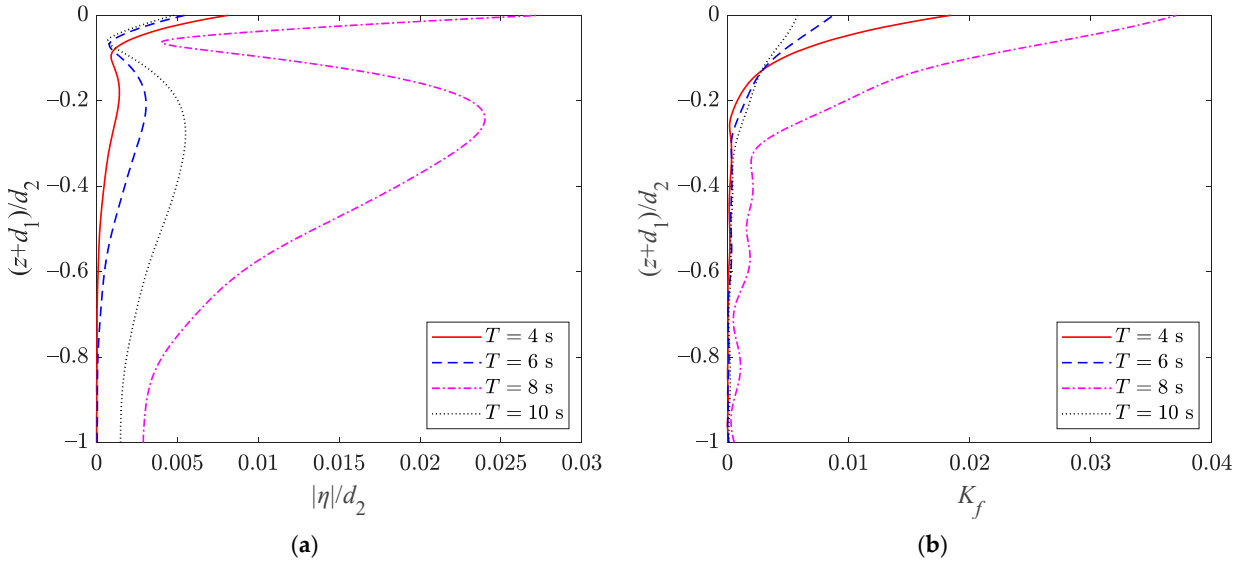

(**a**) (**b**)

Figure 7. (**a**) Nondimensional transverse deflection amplitudes of cage $|\eta|/d_2$, and (**b**) nondimensional horizontal wave load amplitudes per unit length K_f along cage height for various wave periods T, Cases A1 to A4.

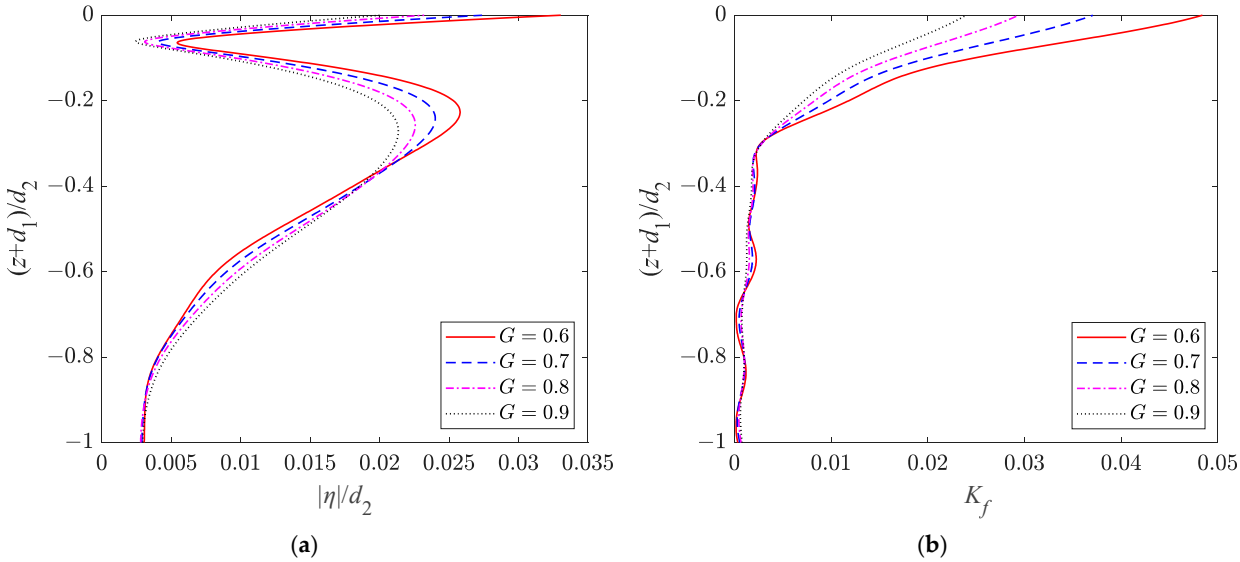

(**a**) (**b**)

Figure 8. (**a**) Nondimensional transverse deflection amplitudes of cage $|\eta|/d_2$, and (**b**) nondimensional horizontal wave load amplitudes per unit length K_f along cage height for various net opening ratios G, Cases B5 to B8.

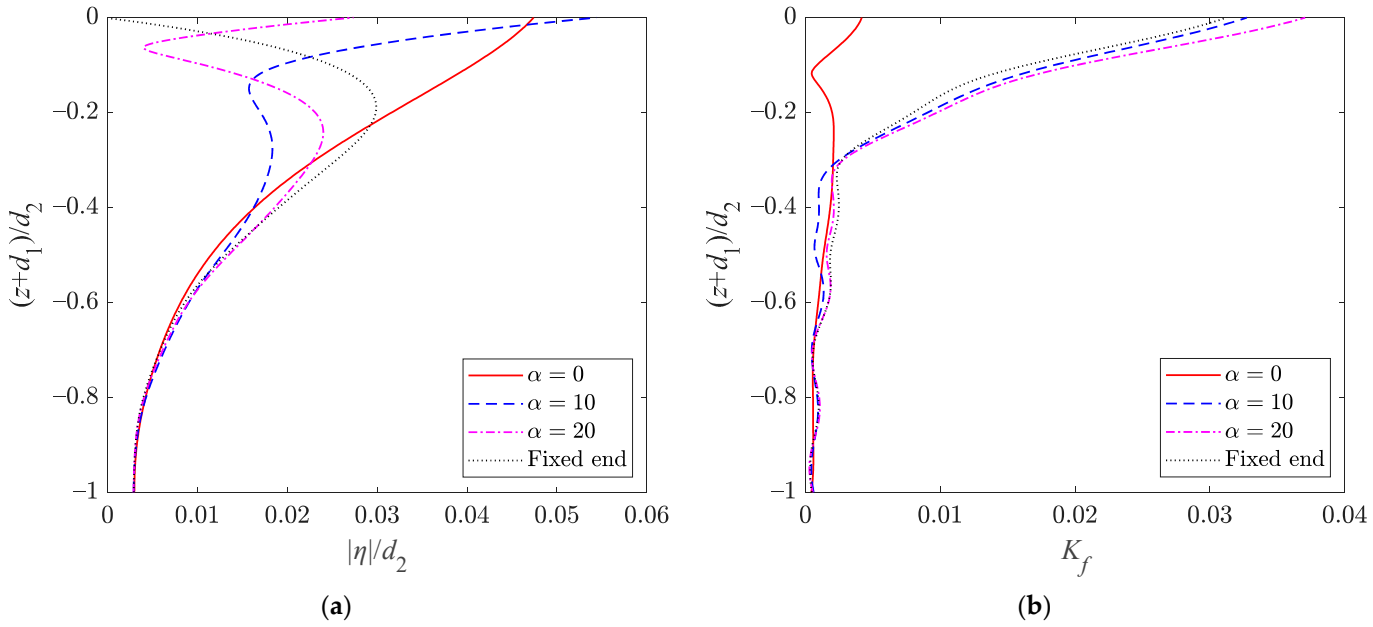

Figure 9. (**a**) Nondimensional transverse deflection amplitudes of cage $|\eta|/d_2$, and (**b**) nondimensional horizontal wave load amplitudes per unit length K_f along cage height for various dimensionless mooring spring constants α, Cases C1 to C4.

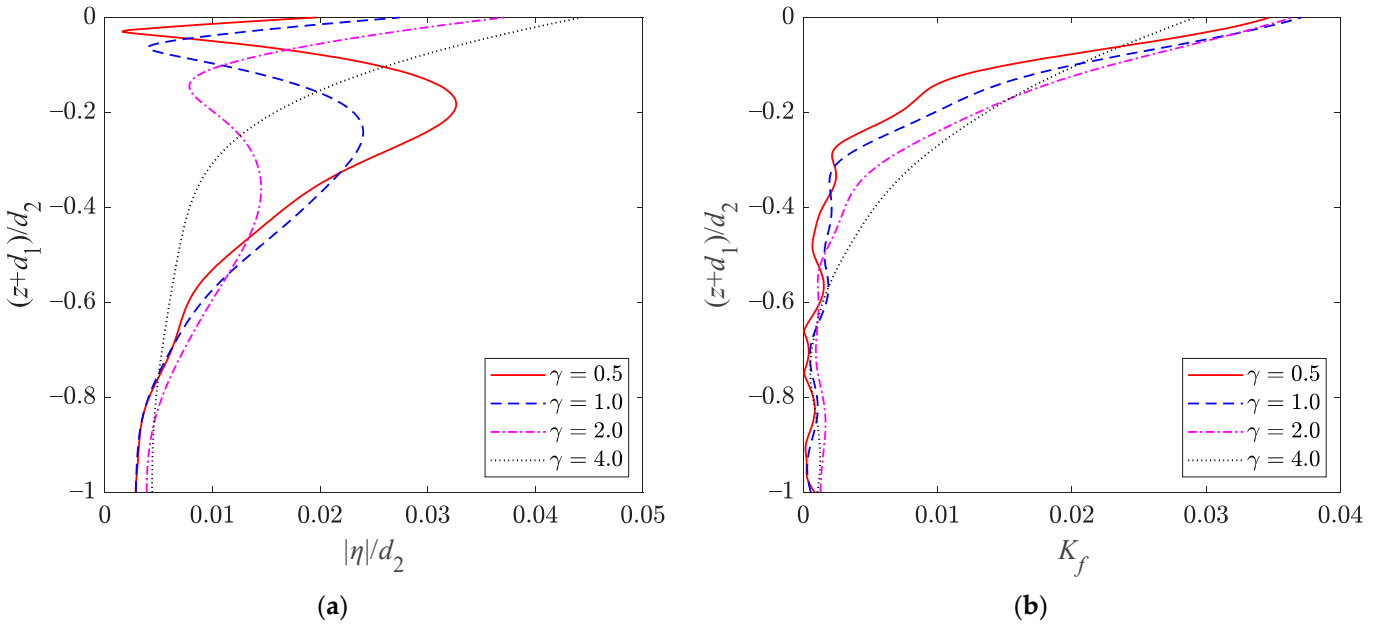

Figure 10. (**a**) Nondimensional transverse deflection amplitudes of cage $|\eta|/d_2$, and (**b**) nondimensional horizontal wave load amplitudes per unit length K_f along cage height for various dimensionless axial tensile forces γ in the net, Cases D1 to D4.

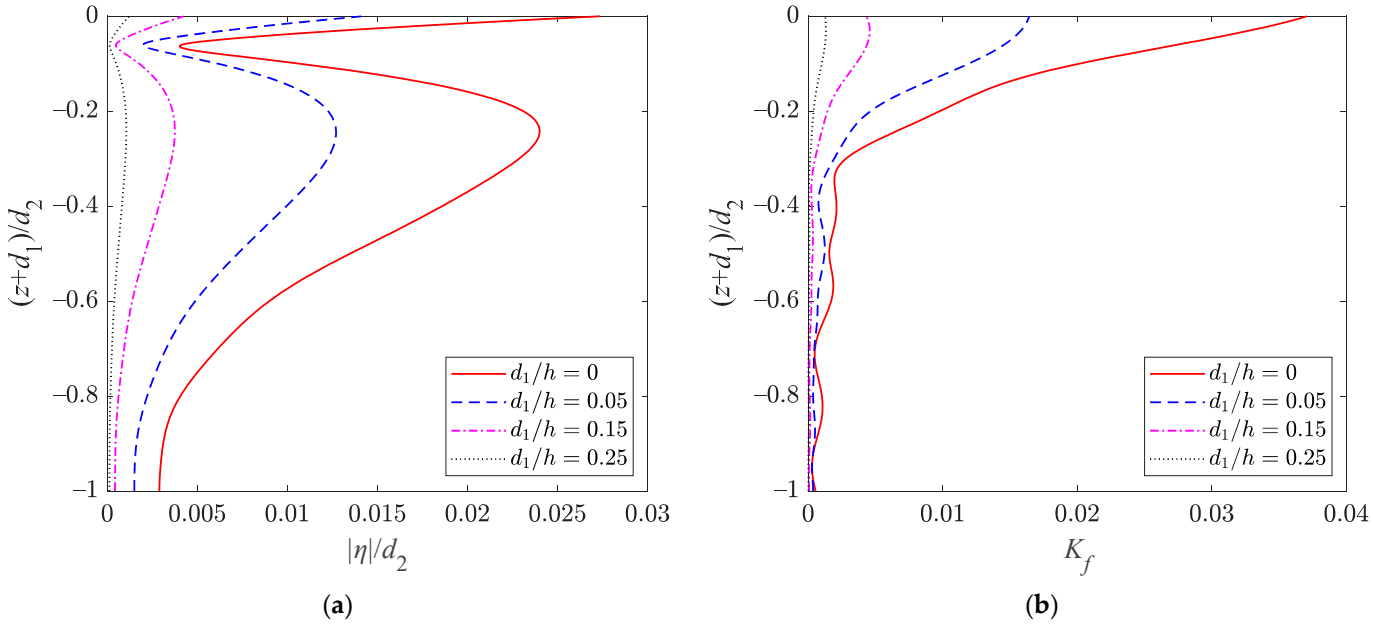

Figure 11. (**a**) Nondimensional transverse deflection amplitudes of cage $|\eta|/d_2$, and (**b**) nondimensional horizontal wave load amplitudes per unit length K_f along cage height for various relative diving depths d_1/h of the cage, Cases E1 to E4.

It can be observed that the greater transverse deflection of the cylindrical net chamber occurs at the upper part of the cage height, and the horizontal wave load per unit length is the largest at the top end of the cage. At the bottom end of the structure, the values of $|\eta|/d_2$ and K_f are the smallest. In addition, due to the assumption of structural edge constraints, the cage has a displacement at the top end (mooring constrained end), and the first derivatives to z are 0 at the bottom end (free end) for the curves of $|\eta|/d_2$.

Figure 7 presents the results of Cases A1 to A4 with T varying from 4 s to 6 s with an interval of 2 s. It can be seen that when T = 8 s, the transverse deflection and wave load on the structure are much greater than the values of the other periods. That indicates that the net cage structure has a critical dynamic response at specific wave frequencies.

In Figure 8, Cases B5 to B8, when the porosity of the fish net increases, the transverse deflection amplitude at the upper part of the net chamber decreases but the value of the lower part slightly increases. With regard to the coefficient K_f, the values at the upper part of the cage have a greater difference, but when $(z + d_1)/d_2$ is smaller than -0.3, these differences are relatively small. This is because these cases are set as floating conditions, and the porous effect of the fish net will have a more significant blocking impact on the flow close to the wave surface.

In Figure 9, Cases C1 to C4 show the effect of the mooring cable stiffness, and there is also a fixed end case ($\eta = 0$ at $z = -d_1$) presented. When $\alpha = 0.5$, a weak spring stiffness results in the vanishing of peaks on the curves of $|\eta|/d_2$ and a significant reduction of the normalized wave load K_f. Nevertheless, when $\alpha > 10$, its influence on wave action becomes relatively minor.

Referring to Figure 10 (Cases D1 to D4), the distribution characteristics of $|\eta|/d_2$ and K_f are similar when $\gamma < 4$. If the axial tension in the cage increases, the overall deformation of the cage can be suppressed, but the top displacement will increase. When $\gamma = 4$, there are no peaks along the curves of $|\eta|/d_2$. Moreover, the wave action is enhanced to a certain extent for a stiffer net cage.

In Figure 11 (Cases D1 to D4), it can be seen that the wave effect will gradually become minimal as the diving depth of the cage increases. The corresponding structural deformation and wave load are also reduced significantly. This justifies the submergence of the cage into a deeper water level to avoid the strong surface waves. Moreover, the 3D shapes of the net chamber with the maximum deformation are plotted at different submerged

depths in Figure 12, where the deflection values are magnified by an exaggerated scale of 5 times. Little wave response of the cage is observed when it is submerged at $d_1/h = 0.25$.

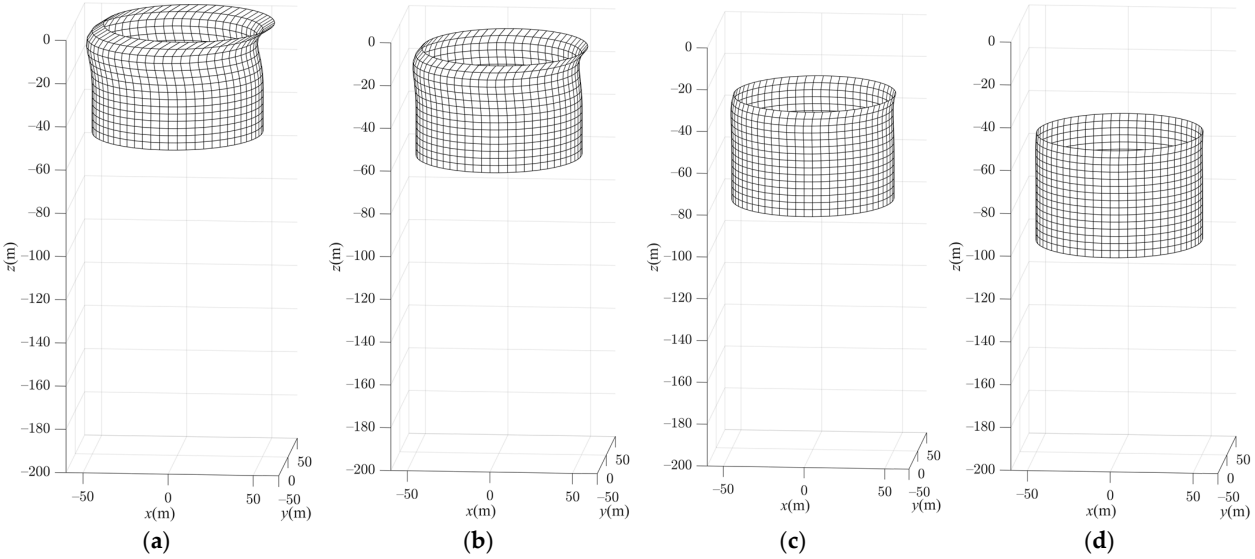

Figure 12. Three-dimensional (3D) shapes of a net cage at different submerged depths with the maximum deformation in an exaggerated scale of 5 times: (**a**) $d_1/h = 0$. (**b**) $d_1/h = 0.05$. (**c**) $d_1/h = 0.15$. (**d**) $d_1/h = 0.25$.

6. Parametric Study

In order to investigate the effects of hydrodynamic and structural parameters on the wave loads, parametric studies are conducted in this section. The nondimensional amplitude of the hydrodynamic force K_F in the horizontal direction and the nondimensional amplitude of the overturning moment K_M with respect to the cage top are defined similarly to Mandal and Sahoo [21]:

$$K_F = \frac{|F|}{\rho g a H h} \text{ and } K_M = \frac{|M_o|}{\rho g a H h (d_1 + d_2)}, \tag{34}$$

in which the wave force F and the resulting overturning moment M_o are found from Equation (29). In the parametric studies, the following nondimensional hydrodynamic parameters are defined: the wave-effect parameter $C_w = g/(\omega^2 h)$ defined by Chwang [11], the incident wave steepness H/L, and the relative water depth h/L, where L is the incident wavelength. The parameters related to the cage dimensions include the relative diameter of the cage $2a/L$, the relative dividing depths of the cage d_1/h, and the relative height of the cage d_2/h. Furthermore, the structural parameters have the nondimensional mooring spring constant α, the nondimensional axial tensile force in the net γ, the nondimensional net mass per unit length β, and the net opening ratio G.

6.1. Hydrodynamic Conditions

The relationship between the wave load on the cage and the wave frequency is given in Figure 13. The curves of K_F and K_M versus C_w show multiple peak points and zero points. This may be because when the wavelength is at a specific value, the phase difference between the scattered waves in the outer region and the inner region near the circular cage is 180 degrees, resulting in wave attenuation. Conversely, if the phase difference is small, the wave action will be strengthened at this frequency.

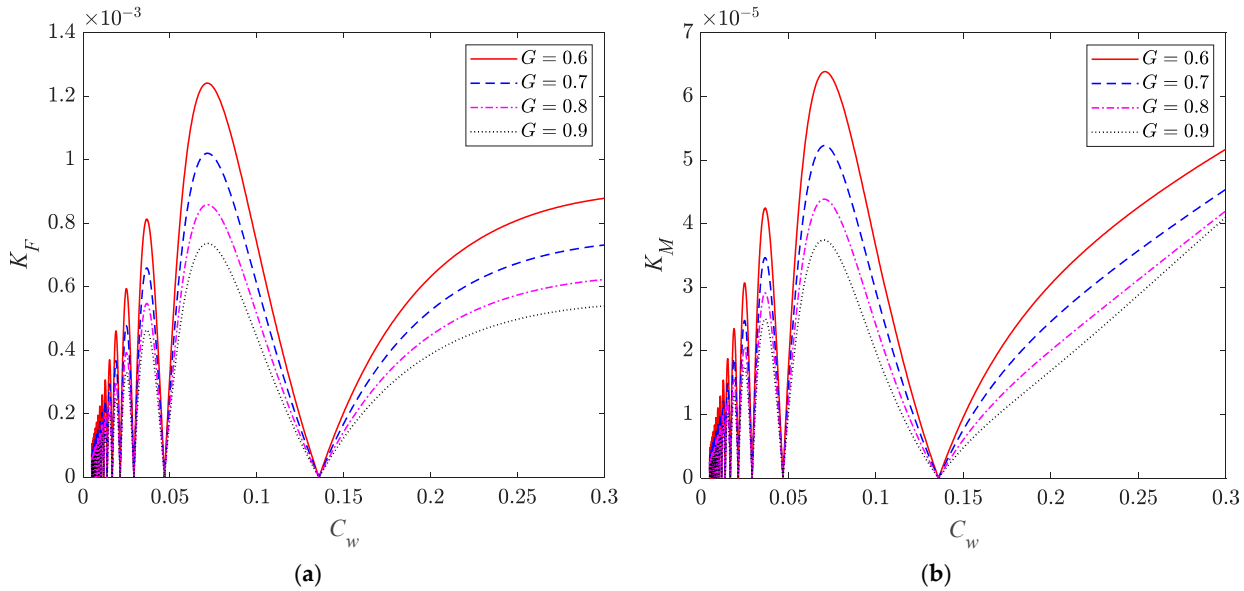

Figure 13. Effect of wave-effect parameter C_w on (**a**) nondimensional amplitude of horizontal hydrodynamic force K_F and (**b**) nondimensional amplitude of horizontal overturning moment K_M for various net opening ratios G, H = 7 m, h = 200 m, a = 50 m, d_1 = 0 m, d_2 = 50 m, α = 20, γ = 1, and β = 0.001.

As shown in Figure 14, the coefficients K_F and K_M are firstly decreased to the minimum values with the relative wave height H/L, and then they start to increase. In the small-amplitude wave theory, the velocity of the water particle has a linear relationship with the wave height. However, Equation (8b) indicates that the real part σ_r of the porous-effect parameter σ is changed related to the varied incident wave slope $\varepsilon = Hk_0/2$. As a result, the wave load acting on the fish net does not increase linearly with the wave height.

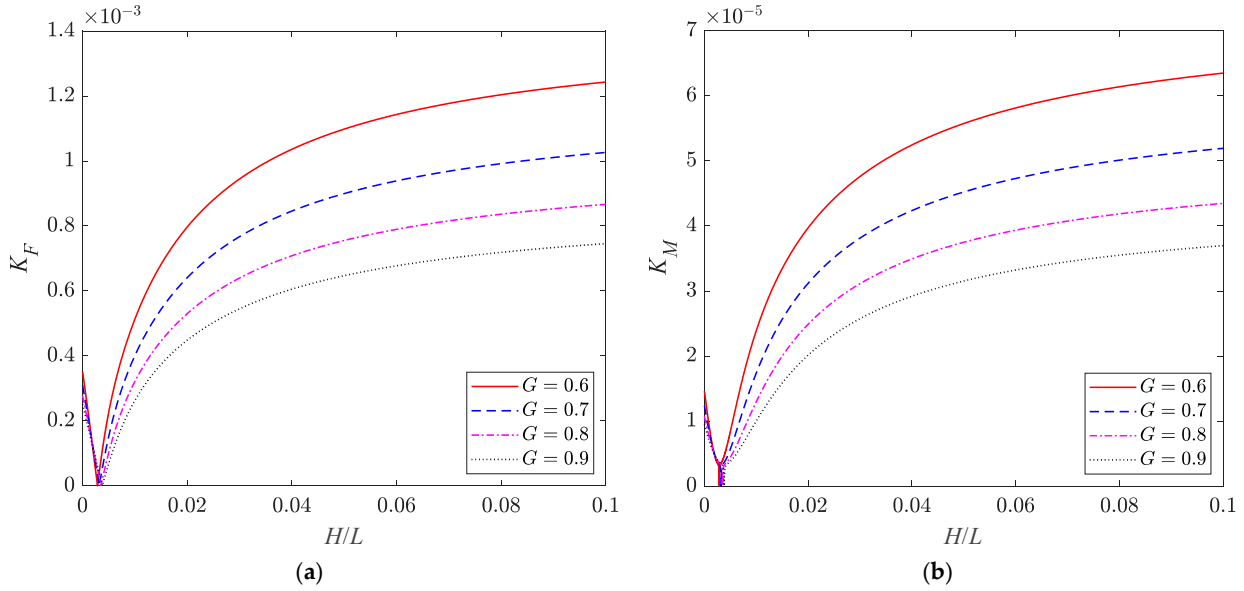

Figure 14. Effect of incident wave steepness H/L on (**a**) nondimensional amplitude of horizontal hydrodynamic force K_F and (**b**) nondimensional amplitude of horizontal overturning moment K_M for various net opening ratios G, T = 8 s, h = 200 m, a = 50 m, d_1 = 0 m, d_2 = 50 m, α = 20, γ = 1 and β = 0.001.

Referring to Figure 15, when the water depth h increases from the values of the cage height to twice the wavelength, the values of K_F and K_M will decrease in opposition to the increase in the relative water depth h/L. It is worth noting that the water depth h is the

denominator in the definition of the coefficients K_F and K_M, which may also contribute to the decrease in the values.

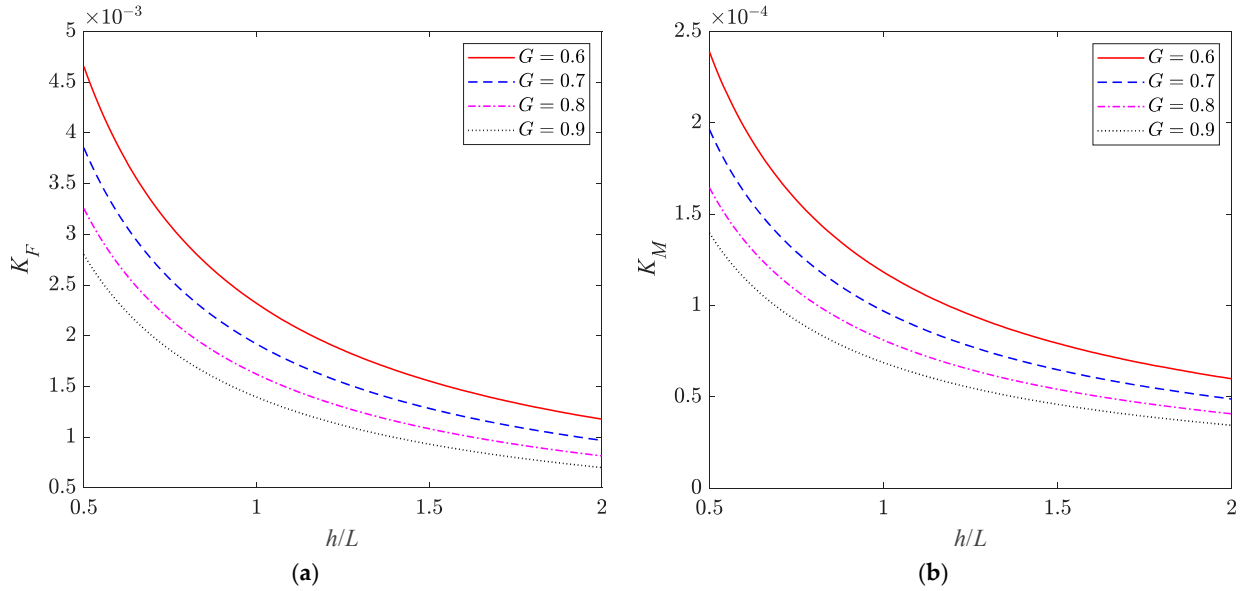

Figure 15. Effect of relative water depth h/L on (**a**) nondimensional amplitude of horizontal hydrodynamic force K_F (**b**) nondimensional amplitude of horizontal overturning moment K_M for various net opening ratios G, T = 8 s, H = 7 m, a = 50 m, d_1 = 0 m, d_2 = 50 m, α = 20, γ = 1, and β = 0.001.

6.2. Cage Dimensions

As illustrated in Figure 16, at a constant wavelength, by increasing the diameter of the cage, the curves of the coefficients K_F and K_M will experience multiple peak points and zeros points as well, where the hydrodynamic force will vanish when $2a/L$ is around 0.59 and 1.70. The wave force on the cylindrical cage has a similar variation under various wave frequencies. Therefore, the ratio of the diameter of the circular cage to the wavelength is crucial in engineering design.

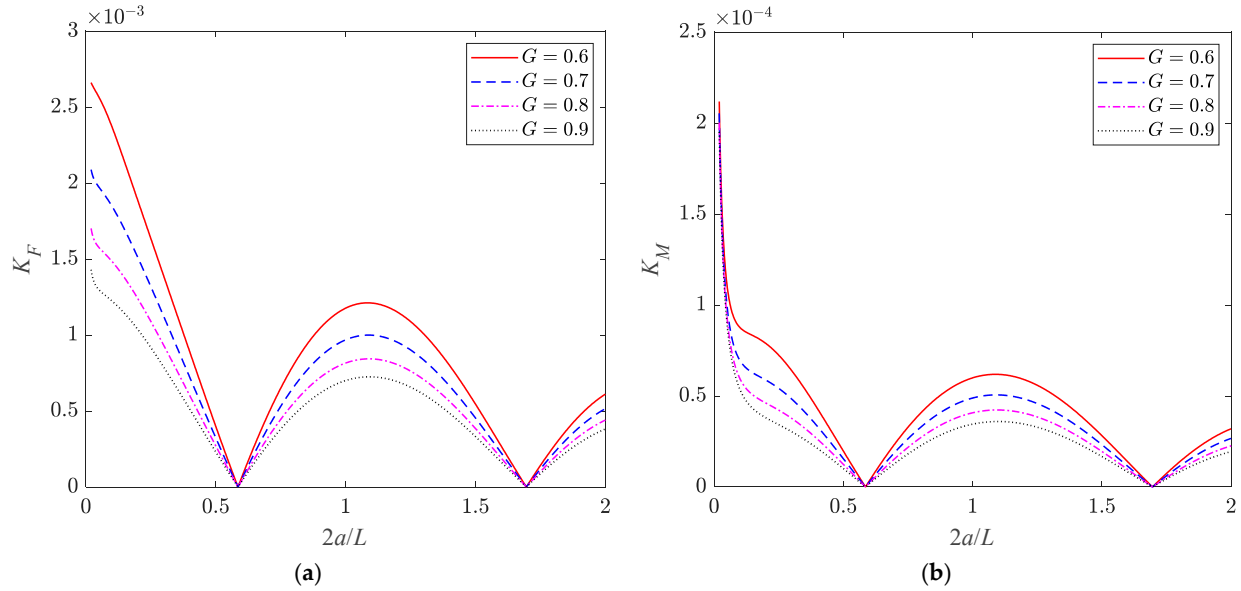

Figure 16. Effect of relative cage diameter $2a/L$ on (**a**) nondimensional amplitude of horizontal hydrodynamic force K_F and (**b**) nondimensional amplitude of horizontal overturning moment K_M for various net opening ratios G, T = 8 s, H = 7 m, h = 200 m, d_1 = 0 m, d_2 = 50 m, α = 20, γ = 1, and β = 0.001.

If the cage is submerged to a deeper location underwater, the effect of surface waves will be weakened, so the coefficients K_F and K_M will be reduced in Figure 17. However, this decreasing trend will slow down as the wave action has been minimal at extremely deep water levels.

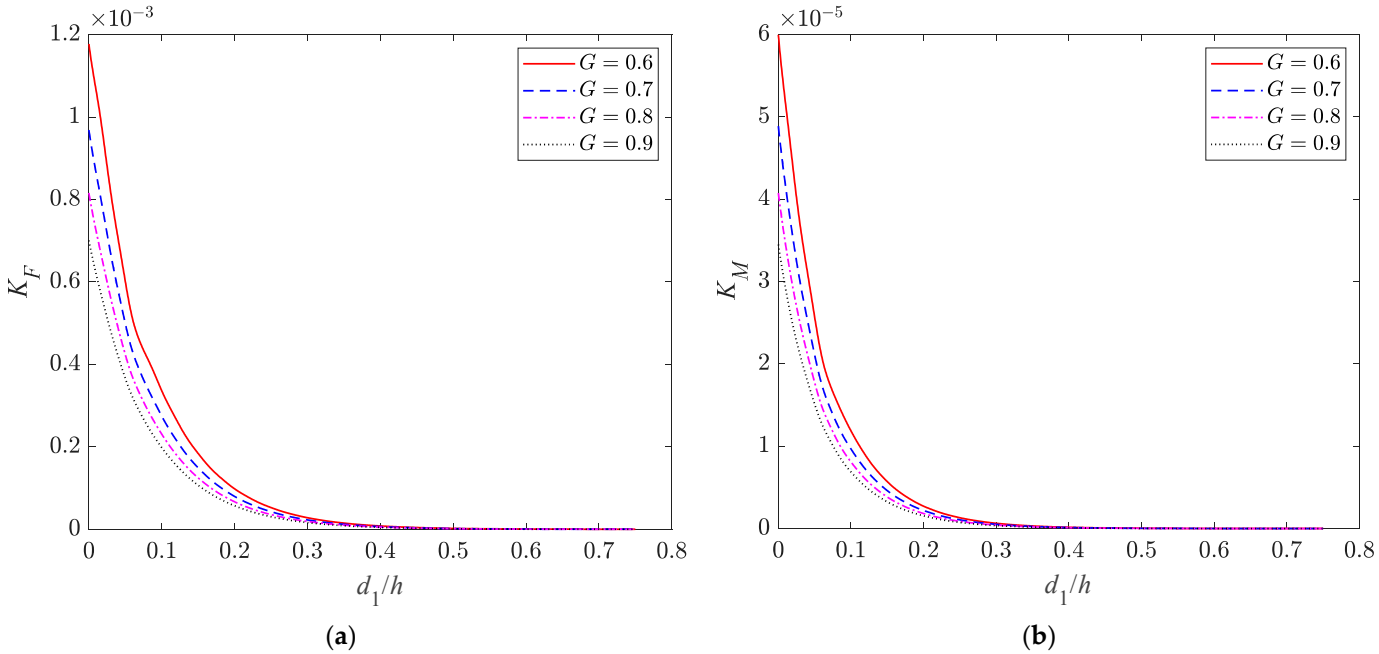

Figure 17. Effect of relative cage diving depth d_1/h on (**a**) nondimensional amplitude of horizontal hydrodynamic force K_F and (**b**) nondimensional amplitude of horizontal overturning moment K_M for various net opening ratios G, T = 8 s, H = 7 m, h = 200 m, a = 50 m, d_2 = 50 m, α = 20, γ = 1, and β = 0.001.

The effect of cage height on the wave load is shown in Figure 18. Attentively, as the cage height d_2 increases, the axial tensile force Q and the mass per unit length m_s of the net chamber will increase if the defined nondimensional parameters γ and β remain constant. This is unreasonable. Therefore, the relevant structural parameters are assumed to take the following values: $Q/(m_s g a) = 1$ and $m_s/(\rho a^2) = 0.001$. Assuming that the top of the cage is at the mean water level, with the increase of the cage height, the values of K_F and K_M will rapidly rush to the peak point, and then begin to decrease. The magnitude of K_F will remain constant after $d_2/h = 0.2$. This is because the imposed wave pressure has been already negligible at the part of the cage close to the deep water level.

6.3. Structural Parameters

It can be observed from Figure 19 that as the spring stiffness of the mooring rope increases, the wave action coefficients K_F and K_M increase to reach a peak value, and then gradually decrease. When $\alpha > 40$, this trend is also slowed down.

The curves in Figure 20 show that the coefficients K_F and K_M are greater with respect to increasing γ. This might be explained by the fact that more momentum of the fluid is dissipated when impacting on stiffer structures. However, the curves of K_F present a slowdown in the growth trend, but K_M increases approximately linearly when $\gamma > 1$.

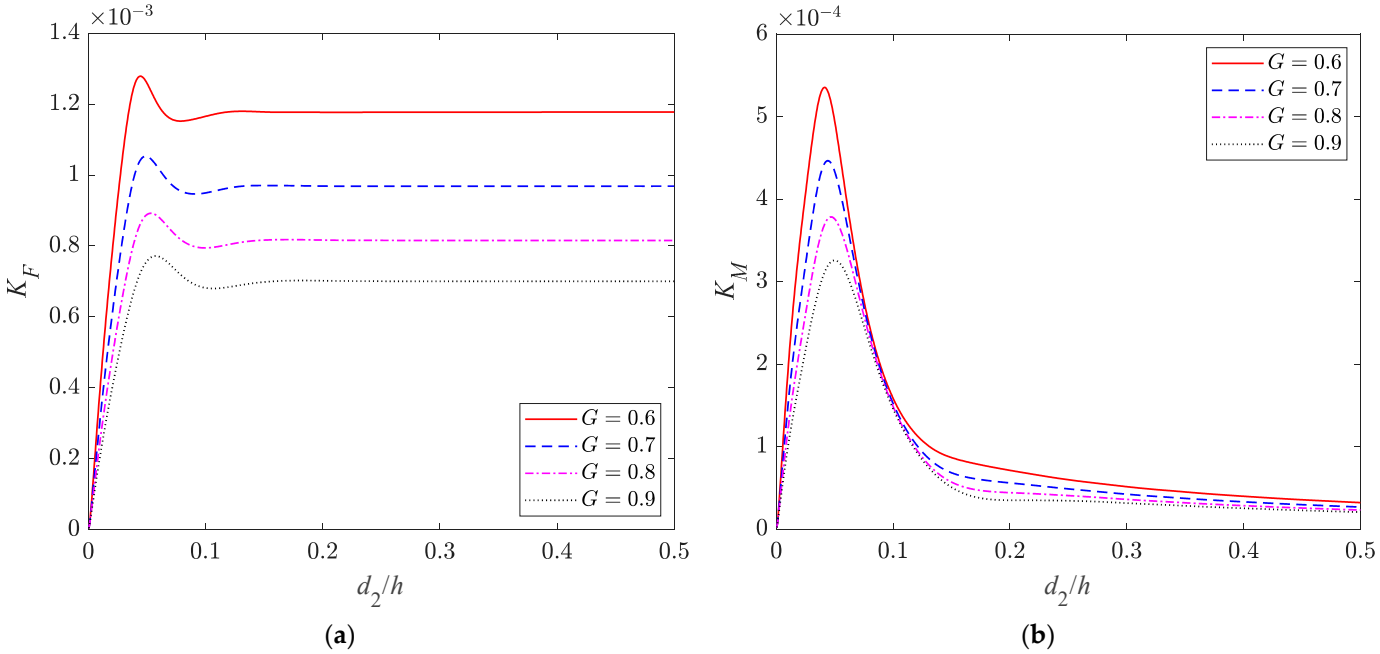

Figure 18. Effect of relative cage height d_2/h on (**a**) nondimensional amplitude of horizontal hydrodynamic force K_F and (**b**) nondimensional amplitude of horizontal overturning moment K_M for various net opening ratios G, T = 8 s, H = 7 m, h = 200 m, a = 50 m, d_1 = 0 m, α = 20, $Q/(m_s g a)$ = 1, and $m_s/(\rho a^2)$ = 0.001.

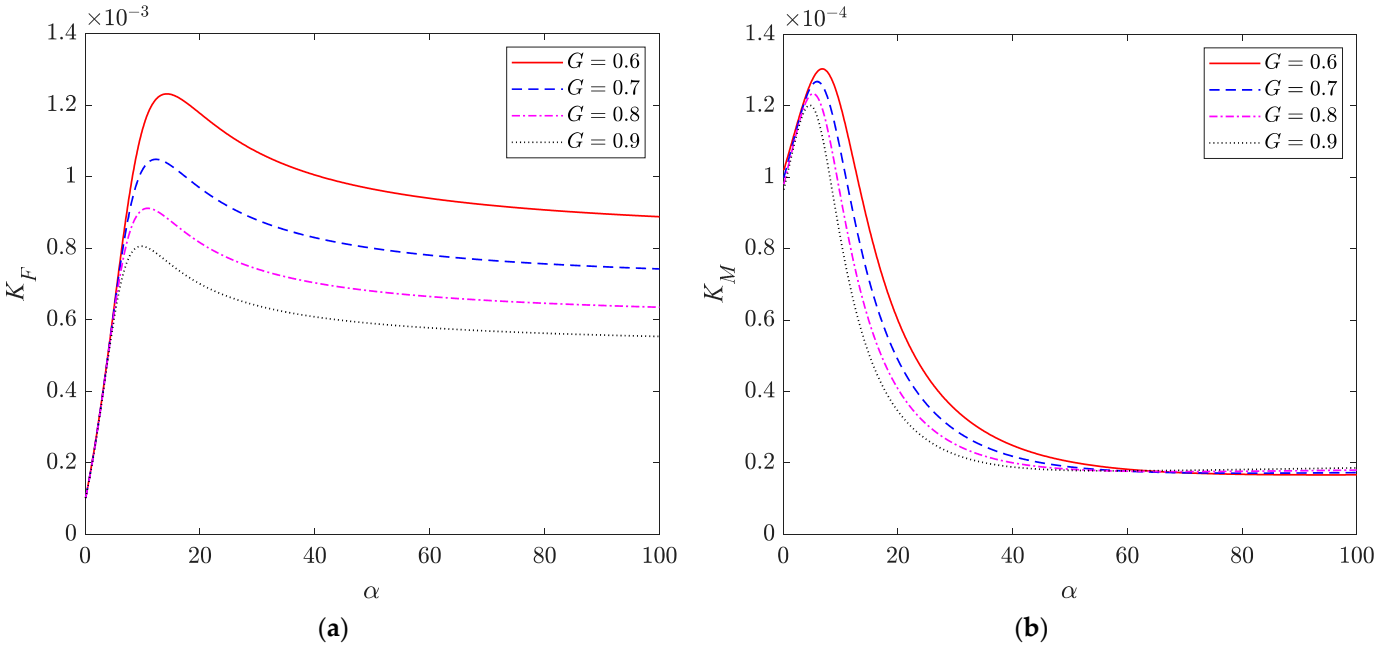

Figure 19. Effect of nondimensional mooring spring constant α on (**a**) nondimensional amplitude of horizontal hydrodynamic force K_F and (**b**) nondimensional amplitude of horizontal overturning moment K_M for various net opening ratios G, T = 8 s, H = 7 m, h = 200 m, a = 50 m, d_1 = 0 m, d_2 = 50 m, γ = 1, and β = 0.001.

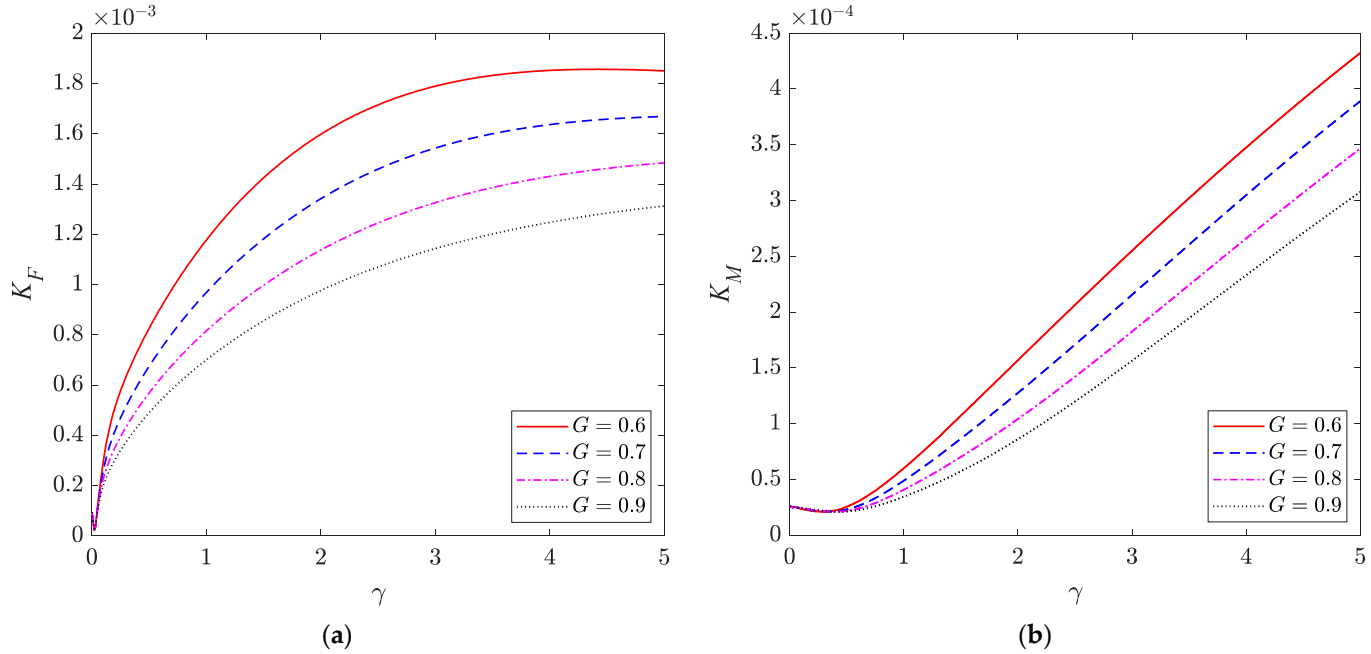

Figure 20. Effect of nondimensional axial tensile force γ in the net on (**a**) nondimensional amplitude of horizontal hydrodynamic force K_F and (**b**) nondimensional amplitude of horizontal overturning moment K_M for various net opening ratios G, T = 8 s, H = 7 m, h = 200 m, a = 50 m, d_1 = 0 m, d_2 = 50 m, α = 20, and β = 0.001.

The mass of the fish net is generally determined by different net materials or biomass effects. In Figure 21, in order to ensure a constant mooring stiffness and axial tension in the net, we have taken that $k_s/(\rho g {d_2}^2) = 0.02$ and $Q/(\rho g {d_2}^3) = 0.001$. It can be observed that, with increasing β from 0 to 0.01, the wave force coefficient K_F initially decreases and then increases slowly, but the moment coefficient K_M decreases slightly first and then increases rapidly.

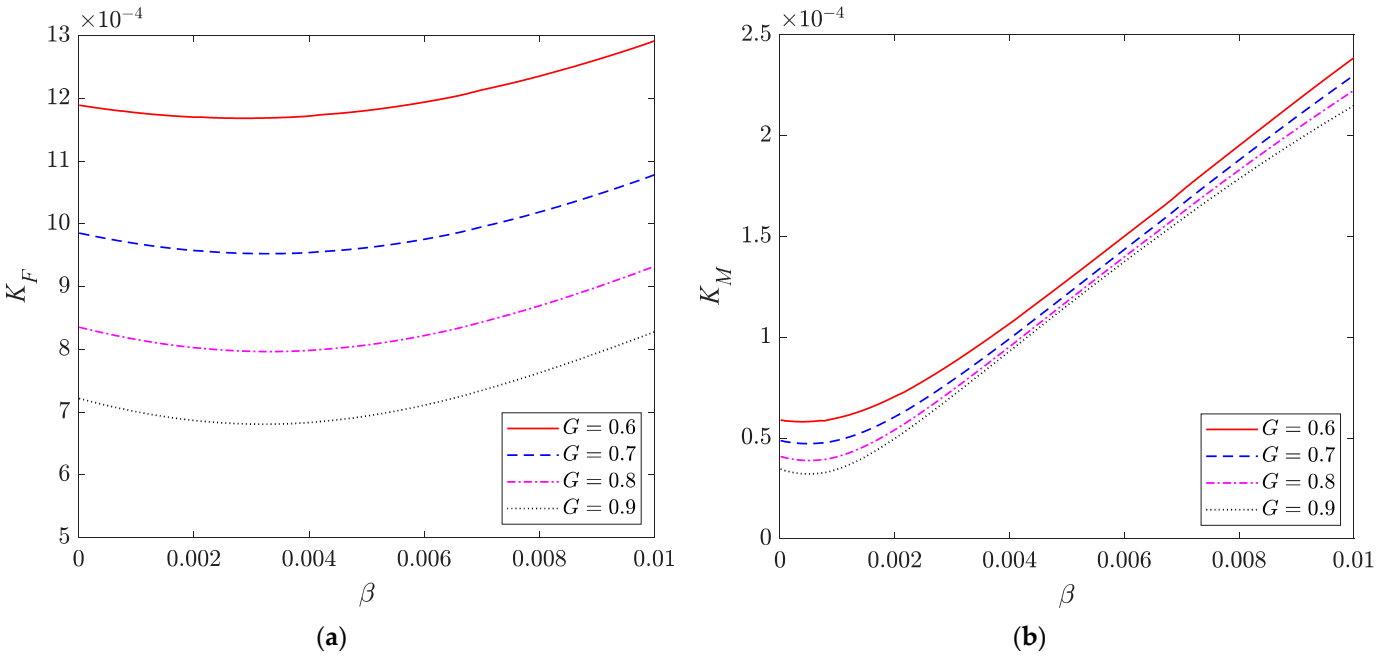

Figure 21. Effect of nondimensional net mass per unit length β on (**a**) nondimensional amplitude of horizontal hydrodynamic force K_F and (**b**) nondimensional amplitude of horizontal overturning moment K_M for various net opening ratios G, T = 8 s, H = 7 m, h = 200 m, a = 50 m, d_1 = 0 m, d_2 = 50 m, $k_s/(\rho g {d_2}^2) = 0.02$, and $Q/(\rho g {d_2}^3) = 0.001$.

In Figure 22, under different axial tensions in the net, the coefficients K_F and K_M show different varying trends when $G < 0.4$. However, the increase in the porosity of the fish net is conducive for reducing the wave action when the opening ratio is over 0.4. Consequently, it is important that the porosity of the net is kept high, and it is essential to clean the net often to remove the biofouling organisms and hydroids to reduce the wave load on the fish cage. Notably, when the net opening ratio $G = 1$, i.e., the net does not exist, the predicted wave forces are not zero. According to [25], theoretically, the porous effect parameter σ should go to infinity when the net interface becomes completely permeable, but Equation (8b) obviously does not obey this scenario. Therefore, a more suitable formula for the porous effect parameter is required in future studies.

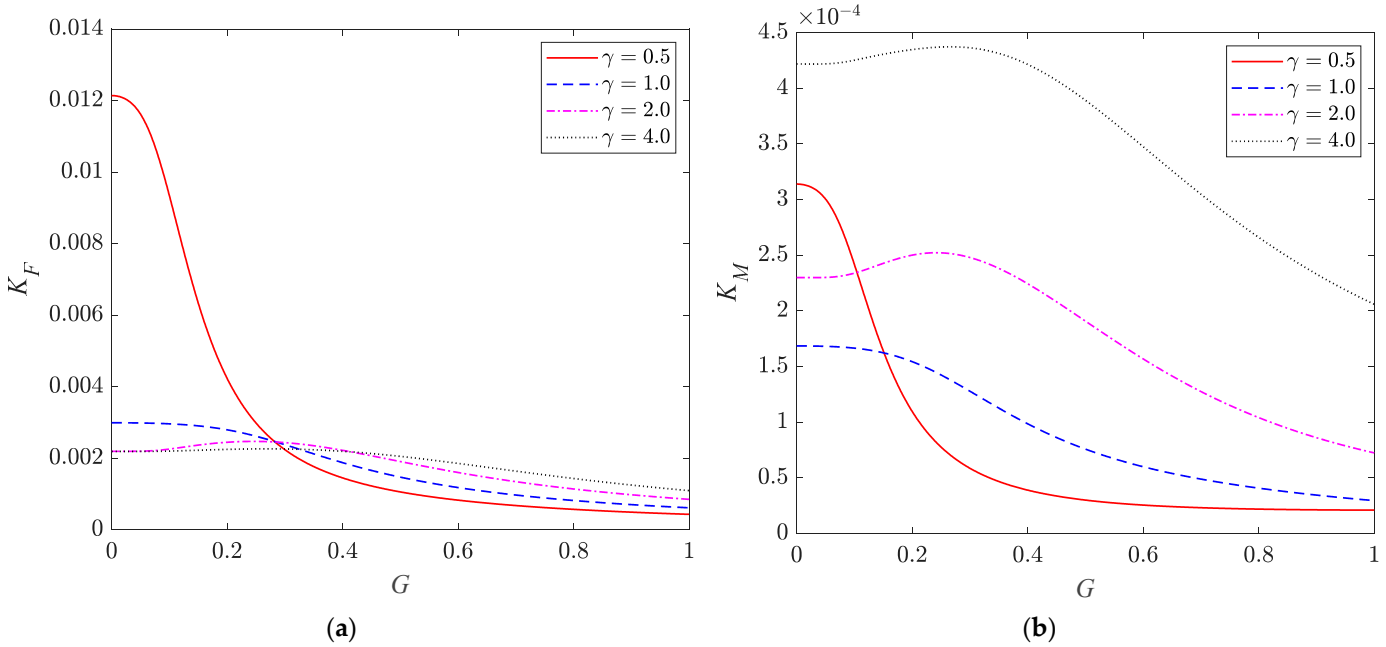

Figure 22. Effect of net opening ratio G on (**a**) nondimensional amplitude of horizontal hydrodynamic force K_F and (**b**) nondimensional amplitude of horizontal overturning moment K_M for various nondimensional axial tensile forces γ in the net, $T = 8$ s, $H = 7$ m, $h = 200$ m, $a = 50$ m, $d_1 = 0$, $d_2 = 50$ m, $\alpha = 20$, and $\beta = 0.001$.

On the other hand, although the assumption in Equation (8a,b) ignores the fluid inertia effect for the flow penetrating through the net interface, its influence still needs to be discussed. An empirical formula of σ_i provided by Ito et al. [25] indicates that most values are in a range of less than 1 for the cube net cage. Here, by assuming that the values of σ_i for most cylindrical net cages are less than 1, the variations of K_F and K_M with respect to σ_i from 0 to 1 are shown in Figure 23. These curves indicate a significant influence of σ_i when the values of γ are high. A minor effect of σ_i is seen when γ is smaller, especially for the coefficient K_M. As a result, the porous effect of the fish net will exhibit different properties with different axial tensions, and thus the fluid inertia effect parameter σ_i still needs further investigation.

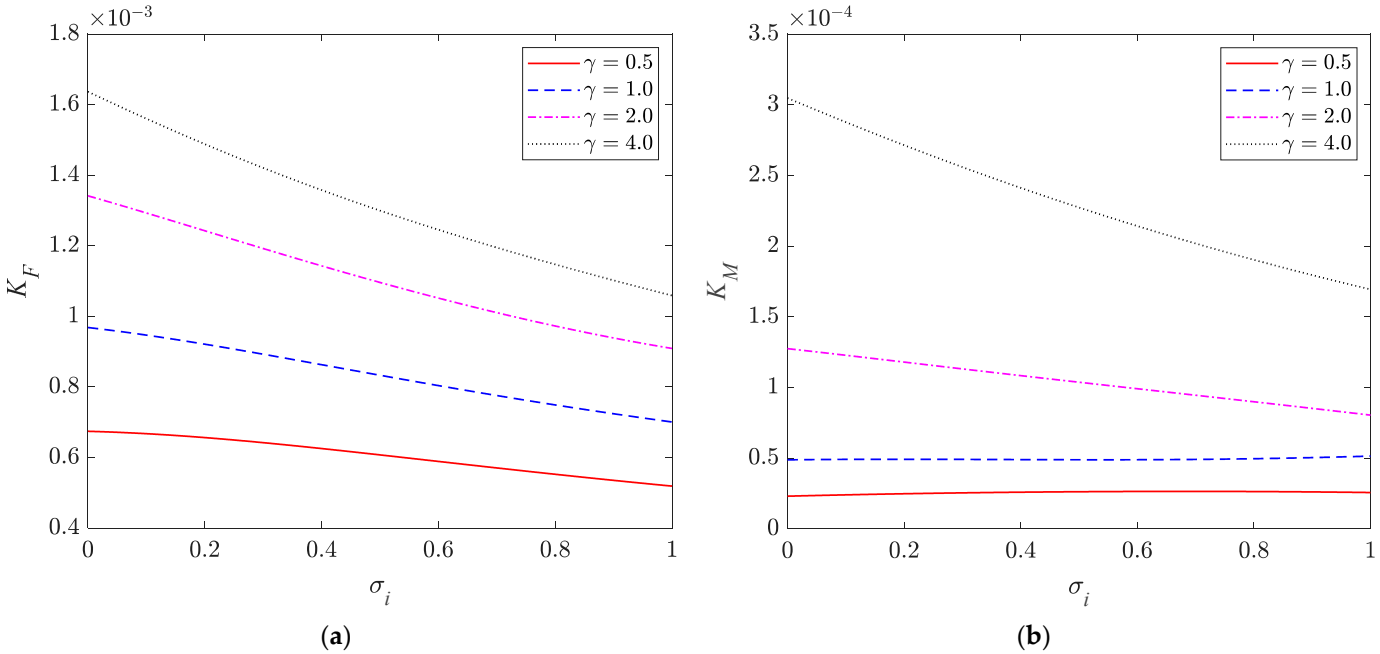

Figure 23. Effect of fluid inertia effect parameter σ_i on (**a**) nondimensional amplitude of horizontal hydrodynamic force K_F and (**b**) nondimensional amplitude of horizontal overturning moment K_M for various nondimensional axial tensile forces γ in the net, T = 8 s, H = 7 m, h = 200 m, a = 50 m, d_1 = 0, d_2 = 50 m, G = 0.7, α = 20, and β = 0.001.

7. Conclusions

A semi-analytical model for wave–cage interaction is established based on the potential flow theory to investigate the hydroelastic behaviour of a cylindrical fish net cage under wave actions. The net cage is modelled as a flexible porous cylinder and its motions are governed by the string vibration equations. By separating variables, the general solution of this physics problem can be expressed by the Fourier–Bessel series. The unknown constants in these series are determined from matching the boundary conditions and the least squares method. Based on this study, the following conclusions may be drawn:

(1) The disturbance caused by the cage to the wave surface is weaker when the opening ratio of the net is greater than 0.3. The wave actions are stronger near the mean water level, as expected. Consequently, a submersible cage is recommended to avoid the high surface-wave energy.
(2) Under different mooring stiffness and axial tension in the net, the deflection amplitude of the cage presents different distribution characteristics.
(3) The net chamber will be subjected to critical wave responses at particular frequencies, but some specific ratios of the cage diameter to the wavelength might cause the vanishing of the wave force and the overturning moment on the cage.
(4) Appropriately increasing the porosity and reducing the axial tension of the net chamber are beneficial in reducing the wave load.
(5) The porous effect of the fish net is significantly impacted by the axial tension in the cage.

The present study reveals some mechanical characteristics of the interaction between the wave and the net cage and provides a reference for the design and application of fish cage systems. However, the theories and formulas used in the present study are all based on linear models, so they cannot solve nonlinear problems in wider scenarios, such as nonlinear waves, quadratic porous flow models, etc., and the structural vibration equation may be oversimplified. Those problems will be considered and resolved in future studies.

Author Contributions: Conceptualization, M.M., H.Z., D.-S.J. and C.M.W.; methodology, M.M.; validation, M.M.; formal analysis, M.M.; writing—original draft preparation, M.M.; writing—review and editing, H.Z., D.-S.J. and C.M.W.; supervision, H.Z., D.-S.J. and C.M.W. All authors have read and agreed to the published version of the manuscript.

Funding: The postgraduate scholarship of Griffith University, Australia, the top-up scholarship of Blue Economy Cooperative Research Centre, Australia and HDR Journal Publishing and Editorial Assistance Scheme (JPEAS) of Griffith Cities Research Institute, Australia.

Data Availability Statement: The main data provided in the present study is generated by the numerical model developed from this paper. For the model validation in Figure 4a, the compared data is from [29] and [30].

Acknowledgments: The first author is very grateful to Griffith University and the Blue Economy CRC for providing scholarships to support this research. In addition, the first author would like to thank Griffith Cities Research Institute for providing HDR Journal Publishing and Editorial Assistance Scheme (JPEAS).

Conflicts of Interest: The authors declare that they have no direct or potential financial and personal relationship with other people or organizations which could inappropriately influence (bias) their work. The authors confirm that the manuscript has been read and approved by all designated authors, and that no one else meets the author criteria but is not listed. We further confirm that the order of authors listed in the manuscript has been approved by all of us.

References

1. FAO. *The State of World Fisheries and Aquaculture 2020*; Food and Agriculture Organization of the United Nations: Rome, Italy, 2020.
2. Zhou, X. Brief Overview of World Aquaculture Production: An Update with Latest Available 2017 Global Production Data. *FAO Aquac. Newslett.* **2019**, *60*, 6–8.
3. Chen, D.; Wang, C.; Zhang, H. Examination of net volume reduction of gravity-type open-net fish cages under sea currents. *Aquac. Eng.* **2021**, *92*, 102128. [CrossRef]
4. Tsukrov, I.; Eroshkin, O.; Fredriksson, D.; Swift, M.; Celikkol, B. Finite element modeling of net panels using a consistent net element. *Ocean Eng.* **2003**, *30*, 251–270. [CrossRef]
5. Zhan, J.; Jia, X.; Li, Y.; Sun, M.; Guo, G.; Hu, Y. Analytical and experimental investigation of drag on nets of fish cages. *Aquac. Eng.* **2006**, *35*, 91–101. [CrossRef]
6. Li, Y.-C.; Zhao, Y.-P.; Gui, F.-K.; Teng, B. Numerical simulation of the hydrodynamic behaviour of submerged plane nets in current. *Ocean Eng.* **2006**, *33*, 2352–2368. [CrossRef]
7. Zhao, Y.-P.; Li, Y.-C.; Dong, G.; Gui, F.-K.; Wu, H. An experimental and numerical study of hydrodynamic characteristics of submerged flexible plane nets in waves. *Aquac. Eng.* **2008**, *38*, 16–25. [CrossRef]
8. Kristiansen, T.; Faltinsen, O.M. Modelling of current loads on aquaculture net cages. *J. Fluids Struct.* **2012**, *34*, 218–235. [CrossRef]
9. Bi, C.-W.; Zhao, Y.-P.; Dong, G.-H.; Xu, T.-J.; Gui, F.-K. Numerical simulation of the interaction between flow and flexible nets. *J. Fluids Struct.* **2014**, *45*, 180–201. [CrossRef]
10. Martin, T.; Tsarau, A.; Bihs, H. A numerical framework for modelling the dynamics of open ocean aquaculture structures in viscous fluids. *Appl. Ocean Res.* **2021**, *106*, 102410. [CrossRef]
11. Chwang, A.T. A porous-wavemaker theory. *J. Fluid Mech.* **1983**, *132*, 395–406. [CrossRef]
12. Yu, X.; Chwang, A.T. Wave-Induced Oscillation in Harbor with Porous Breakwaters. *J. Waterw. Port Coast. Ocean Eng.* **1994**, *120*, 125–144. [CrossRef]
13. Lee, M.M.; Chwang, A.T. Scattering and radiation of water waves by permeable barriers. *Phys. Fluids* **2000**, *12*, 54–65. [CrossRef]
14. Sankarbabu, K.; Sannasiraj, S.; Sundar, V. Interaction of regular waves with a group of dual porous circular cylinders. *Appl. Ocean Res.* **2007**, *29*, 180–190. [CrossRef]
15. Park, M.-S.; Koo, W.-C.; Choi, Y.-R. Hydrodynamic interaction with an array of porous circular cylinders. *Int. J. Nav. Arch. Ocean Eng.* **2010**, *2*, 146–154. [CrossRef]
16. Abul-Azm, A.; Williams, A. Interference effects between flexible cylinders in waves. *Ocean Eng.* **1987**, *14*, 19–38. [CrossRef]
17. Yip, T.; Sahoo, T.; Chwang, A.T. Trapping of surface waves by porous and flexible structures. *Wave Motion* **2002**, *35*, 41–54. [CrossRef]
18. Behera, H.; Sahoo, T. Hydroelastic analysis of gravity wave interaction with submerged horizontal flexible porous plate. *J. Fluids Struct.* **2015**, *54*, 643–660. [CrossRef]
19. Mandal, S.; Datta, N.; Sahoo, T. Hydroelastic analysis of surface wave interaction with concentric porous and flexible cylinder systems. *J. Fluids Struct.* **2013**, *42*, 437–455. [CrossRef]
20. Su, W.; Zhan, J.-M.; Huang, H. Analysis of a porous and flexible cylinder in waves. *China Ocean Eng.* **2015**, *29*, 357–368. [CrossRef]
21. Mandal, S.; Sahoo, T. Gravity wave interaction with a flexible circular cage system. *Appl. Ocean Res.* **2016**, *58*, 37–48. [CrossRef]

22. Selvan, S.A.; Gayathri, R.; Behera, H.; Meylan, M.H. Surface wave scattering by multiple flexible fishing cage system. *Phys. Fluids* **2021**, *33*, 037119. [CrossRef]
23. Guo, Y.; Mohapatra, S.; Soares, C.G. Review of developments in porous membranes and net-type structures for breakwaters and fish cages. *Ocean Eng.* **2020**, *200*, 107027. [CrossRef]
24. Li, M.; Zhang, H.; Guan, H.; Lin, G. Three-dimensional investigation of wave–pile group interaction using the scaled boundary finite element method. Part I: Theoretical developments. *Ocean Eng.* **2013**, *64*, 174–184. [CrossRef]
25. Ito, S.; Kinoshia, T.; Bao, W. Hydrodynamic behaviors of an elastic net structure. *Ocean Eng.* **2014**, *92*, 188–197. [CrossRef]
26. Liu, H.-F.; Bi, C.-W.; Zhao, Y.-P. Experimental and numerical study of the hydrodynamic characteristics of a semisubmersible aquaculture facility in waves. *Ocean Eng.* **2020**, *214*, 107714. [CrossRef]
27. Sommerfeld, A. *Partial Differential Equations in Physics*; Elsevier Science & Technology: Burlington, MA, USA, 1949. [CrossRef]
28. Liu, Z.; Mohapatra, S.; Soares, C. Finite Element Analysis of the Effect of Currents on the Dynamics of a Moored Flexible Cylindrical Net Cage. *J. Mar. Sci. Eng.* **2021**, *9*, 159. [CrossRef]
29. Zhao, F.; Bao, W.; Kinoshita, T.; Itakura, H. Theoretical and Experimental Study on a Porous Cylinder Floating in Waves. *J. Offshore Mech. Arct. Eng.* **2010**, *133*, 011301. [CrossRef]
30. Park, M.-S.; Koo, W. Mathematical Modeling of Partial-Porous Circular Cylinders with Water Waves. *Math. Probl. Eng.* **2015**, *2015*, 903748. [CrossRef]